

Resonant X-ray Scattering in Manganites - Study of Orbital Degree of Freedom -

Sumio Ishihara and Sadamichi Maekawa

† Department of Applied Physics, University of Tokyo, Tokyo 113-8656, Japan

‡ Institute for Materials Research, Tohoku University, Sendai 980-8577, Japan

E-mail: ishihara@ap.t.u-tokyo.ac.jp and maekawa@imr.tohoku.ac.jp

Abstract. Orbital degree of freedom of electrons and its interplay with spin, charge and lattice degrees of freedom are one of the central issues in colossal magnetoresistive manganites. The orbital degree of freedom has until recently remained hidden, since it does not couple directly to most of experimental probes. Development of synchrotron light sources has changed the situation; by the resonant x-ray scattering (RXS) technique the orbital ordering has successfully been observed. In this article, we review progress in the recent studies of RXS in manganites. We start with a detailed review of the RXS experiments applied to the orbital ordered manganites and other correlated electron systems. We derive the scattering cross section of RXS where the tensor character of the atomic scattering factor (ASF) with respect to the x-ray polarization is stressed. Microscopic mechanisms of the anisotropic tensor character of ASF is introduced and numerical results of ASF and the scattering intensity are presented. The azimuthal angle scan is a unique experimental method to identify RXS from the orbital degree of freedom. A theory of the azimuthal angle and polarization dependence of the RXS intensity is presented. The theoretical results show good agreement with the experiments in manganites. Apart from the microscopic description of ASF, a theoretical framework of RXS to relate directly to the $3d$ orbital is presented. The scattering cross section is represented by the correlation function of the pseudo-spin operator for the orbital degree of freedom. A theory is extended to the resonant inelastic x-ray scattering and methods to observe excitations of the orbital degree of freedom are proposed.

Submitted to: *Rep. Prog. Phys.*

<i>CONTENTS</i>	2
Contents	
1 Introduction	3
2 Survey of experiments	6
2.1 Historical background of the observation of orbital and RXS	6
2.2 A variety of recent RXS experiments	8
3 Theoretical framework	14
3.1 Scattering cross section	14
3.2 Microscopic mechanism of RXS in orbital ordered states	18
3.3 Azimuthal angle dependence	27
3.4 General theoretical framework of RXS - orbital ordering, fluctuation and excitations -	33
4 Summary	41
5 Acknowledgements	42

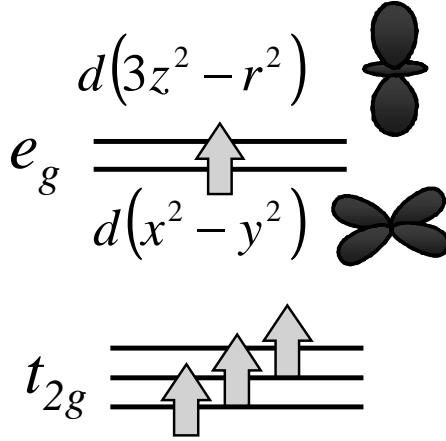


Figure 1. A schematic picture of the energy level in a Mn^{3+} ion and the $3d_{3z^2-r^2}$ and $3d_{x^2-y^2}$ orbitals.

1. Introduction

The discovery of the high T_c superconducting cuprates [1] have stimulated the revival studies of a variety of transition-metal oxides from modern theoretical and experimental view points. Among them, special attention is placed on manganites $A_{1-x}B_x\text{MnO}_3$ [2, 3] with pseudo-cubic perovskite structure and their related materials. Here, A and B are trivalent and divalent cations, respectively. This is owing to the newly discovered colossal magnetoresistance (CMR)[4, 5, 6, 7]: a huge decreasing of the electrical resistivity by applying a magnetic field. As well as CMR, a number of dramatic and fruitful phenomena in magnetic, electric and optical properties has been reported. Some of them can not be explained by the simple double exchange scenario [8, 9, 10, 11] and are ascribed to the strong interplay between spin, charge and orbital degrees of freedom of an electron, as well as lattice [12, 13, 14, 15, 16]. Let us compare the electronic structure in CMR manganites with that in high T_c cuprates. As well as cuprates, manganites are known to be strongly correlated electron systems. In particular, the strong Hund coupling is stressed for origin of the ferromagnetic metallic state. This is so-called the double exchange interaction [17, 18, 19, 20, 21, 22, 23]. The electron configuration of a Cu^{2+} ion in La_2CuO_4 is $3d^9$ and it is located at a center of a tetragonally distorted CuO_6 octahedron. Here, one hole occupies the $3d_{x^2-y^2}$ orbital. On the other hand, four $3d$ electrons in a Mn^{3+} ion form the high spin state, and the electrons occupy the three t_{2g} orbitals and one of the doubly degenerate e_g orbitals as $t_{2g}^3 e_g^1$ (see Fig. 1). Therefore, this ion has a degree of freedom indicating which e_g orbital is occupied by an electron. This is termed the orbital degree of freedom and is recognized as the third degree of

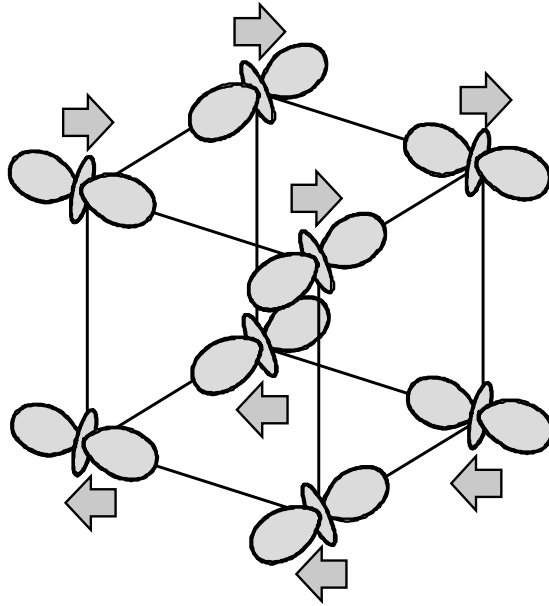


Figure 2. The orbital ordered state in LaMnO_3 . Bold arrows indicate Mn spins.

freedom of an electron, in addition to the spin and charge ones.

In solid, the orbital degree of freedom often shows the long range ordering, termed the orbital ordering, which is caused by the inter-site interaction between orbitals. One of the examples is found in the parent compound of CMR manganites, LaMnO_3 , where $3d_{3x^2-r^2}$ and $3d_{3y^2-r^2}$ orbitals are alternately aligned in the ab plane below 780K (see Fig. 2) [24, 25, 26, 27, 28, 29]. It is widely accepted that this orbital ordering governs the anisotropic spin order termed the A -type antiferromagnetic (AF) order where spins are ferromagnetically aligned in the ab plane and antiferromagnetically along the c axis [26, 30, 31, 32, 33, 34, 35, 36, 37]. Another type of the orbital ordering appears in $A_{0.5}B_{0.5}\text{MnO}_3$ where a nominal valence of a Mn ion is $3.5+$ [30, 38, 39, 40, 41, 42, 43, 44]. Below a certain temperature, Mn^{3+} and Mn^{4+} ions spatially order and, in the Mn^{3+} sublattice, two kinds of orbital sublattice appear. The charge and orbital orderings occur at the same temperature and, at finally, the spin order termed the CE-type AF order is realized. Thus, all electronic degrees of freedom are frozen in the low temperature phase. Since CMR appears at the vicinity of the charge and orbital ordering transition, it is recognized that the orbital plays a crucial role on CMR and other dramatic phenomena in manganites.

Theoretical study of the electronic orbital in $3d$ electron systems is retrospective to more than 40 years ago. Signs and magnitudes of the superexchange interactions have been studied in the systems with orbital degeneracy in 1950's [45, 26, 46]. The

orbital degeneracy brings about the ferromagnetic interaction between same kinds of ions in the case where an angle of the bond connecting the nearest neighboring (NN) magnetic ions is 180° . As well as the superexchange interaction between spins, the virtual exchanges of electrons under the strong Coulomb interactions induce the inter-site interactions between orbitals. Being based on the theoretical models, where spin and orbital are treated on an equal footing, the mutual relations between spin and orbital orderings were investigated in several magnetic compounds [47, 48, 49, 50, 51, 52, 53, 54]. On the other hand, the orbital ordering has been studied in connection with Jahn-Teller effects. In molecules, a degeneracy of electronic orbitals is always lifted spontaneously by lowering symmetry of molecule except for chain-shaped molecules. This is the Jahn-Teller theorem [55]. In solid, the virtual exchange of phonons brings about the inter-site interaction between orbitals and causes the orbital ordering associated with the structural phase transition. This is termed the cooperative Jahn-Teller effects [56, 57, 58, 59]. After the discovery of CMR, theoretical study of the orbital degree of freedom has been revived and, in particular, the following new points of researches are focused on: (1) dynamics of the orbital degree of freedom [34, 35, 60, 61, 62, 63, 64, 65, 66], (2) roles of the orbital on magnetic, transport and optical properties in metals [67, 68, 69, 70, 71, 72, 73, 74, 75, 76, 77, 78, 79, 80, 81], and (3) exotic orbital ordered states [82, 83, 84, 85, 86, 87, 88]. Actually, a variety of orbital states was proposed theoretically in manganites and other transition-metal oxides. However, direct comparisons of these predictions with experimental results have been limited up to recently, because the orbital degree of freedom does not couple directly to most of experimental probes. This is in contrast to the spin and charge degrees of freedom which are directly detected by the neutron and electron/x-ray diffraction techniques, respectively.

In 1998, Murakami and coworkers applied the resonant x-ray scattering (RXS) method to one of the orbital ordered manganites $\text{La}_{0.5}\text{Sr}_{1.5}\text{MnO}_4$ and successfully observed the orbital order [89]. This technique has been rapidly developed and expanded to several compounds with orbital degree of freedom. Nowadays, RXS uncovers a whole feature of the spin-charge-orbital coupled systems. In this article, we review the recent progress of the theoretical and experimental developments of RXS in manganites.

In Sec. 2.1, histories of the observation of the orbital and RXS are introduced. The recent experimental results of RXS are reviewed in Sec. 2.2. Section 3 is devoted to the review of the theoretical study of RXS. We derive the scattering cross section of RXS and stress the anisotropy of the atomic scattering factor (ASF) in Sec. 3.1. Microscopic mechanisms of the anisotropy of ASF in orbital ordered state is introduced in Sec. 3.2. The azimuthal angle scan is a unique experimental method by which RXS from the orbital ordering is identified. A theory of the azimuthal angle and polarization dependence of RXS is presented in Sec. 3.3. Apart from the microscopic mechanisms of the anisotropy of ASF, we introduce, in Sec. 3.4, the general theoretical framework of RXS where the scattering cross section is directly related to the orbital degree of freedom. This is applied to study of the orbital ordering, fluctuation and excitations.

Section 4 is devoted to the summary.

2. Survey of experiments

2.1. Historical background of the observation of orbital and RXS

Experimental observation of the orbital degree of freedom of an electron is, in general, a hard task, unlike spin, charge and lattice degrees of freedom. As mentioned previously, in molecules, a degeneracy of electronic orbitals is lifted by the Jahn-Teller effects. It may be expected that, also in solid, the orbital ordering always occurs by a crystal lattice distortion as known to be the cooperative Jahn-Teller effects. Even when the orbital ordering is caused by other mechanisms, the crystal lattice may follow a shape of the electronic cloud by the electron-lattice interactions. Thus, one may think that the orbital ordering can be observed through measuring the lattice distortion. However, this is not always true and one to one correspondence between orbital and lattice does not exist in solid. This is because there is an infinite number of degrees of freedom and several interactions acting on orbital and lattice compete and cooperate with each other.

In principle, the scattering intensities in the several diffraction experiments depend on the anisotropic shape of the electronic wave function and/or electronic charge distribution. However, since the orbital dependence of the scattering intensity is too small to be observed easily, precise experiments in a wide range of diffraction angles and detailed data analyses are required. As an example, let us consider the conventional x-ray diffraction experiments. The peak intensity is proportional to the square of the electronic charge valence. On the other hand, a difference of the electronic orbital corresponds to a difference of the charge valence being less than a charge unit e . Thus, the orbital effects in the x-ray scattering intensity is usually smeared out by the scatterings from heavy ions, impurities, defects and so on. The first direct observation of the orbital ordered state was carried out by the polarized neutron diffraction method in K_2CuF_4 [90, 91]. This technique is applicable to the observation of orbital ordering in magnetically ordered state where both the spin and orbital moments are ascribed to the same d or f electrons. The magnetic structure factors f_M which include information of the electronic orbital are measured at several reflection points and are compared with the model calculations. This method was recently applied to the ferromagnetic YTiO_3 and revealed successfully the type of the orbital ordered state [92]. Another experimental observation of the orbital ordering was carried out by the charge density distribution study using the x-ray and/or electron diffraction technique. The charge density of a Cu^+ ion in Cu_2O was recently observed by utilizing the convergent-beam electron diffraction combined with x-ray diffraction [93]. In general, x-ray scattering is sensitive to defects contained in a crystal and the scattering from defects is greater than the orbital dependent scattering. Thus, a perfect region of a crystal is selected by the electron microscopy and the charge distribution map is obtained by the electron

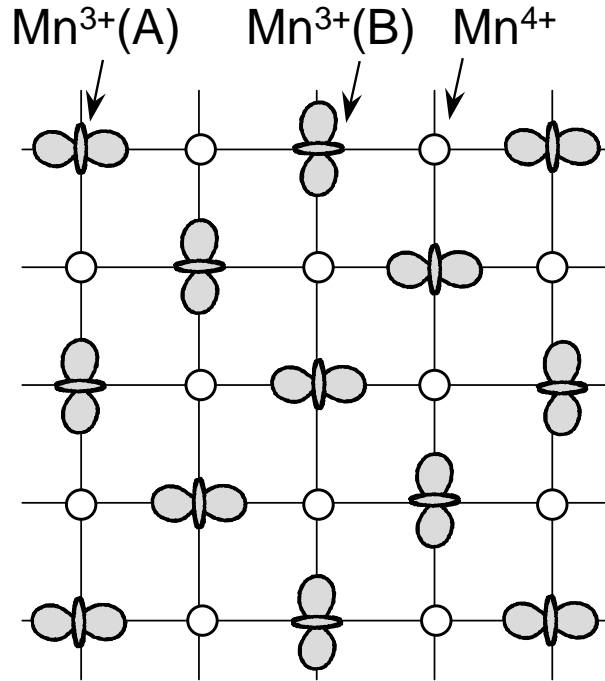


Figure 3. The charge and orbital ordered state in the ab plane of $\text{La}_{1.5}\text{Sr}_{0.5}\text{MnO}_4$. Open circles indicate Mn^{4+} ions [89].

and x-ray diffraction data in a wide region of scattering angles. An electronic charge-distribution is also obtained by the combined method of the Rietveld refinement of the x-ray powder diffraction data and the maximum entropy method (MEM). Here, MEM is utilized to construct a real space charge-distribution from the x-ray diffraction data by the Fourier transformation. This method has been applied to the structural studies of several fullerene and silicides, [94, 95] and was recently applied to $\text{NdSr}_2\text{Mn}_2\text{O}_7$ [96].

The study of the resonant x-ray scattering and anisotropic character of the x-ray scattering have been developed in the research field of the crystallography more than twenty years ago. The anisotropies of absorption and reflection in the visible light regions, i.e. the linear dichroism and birefringence (double reflection), are well known phenomena and useful to the study of the electronic structure in solid. However, in the x-ray region, these are usually small and the scattering factor is treated as a scalar with respect to the polarization of x ray. The observations of the polarization dependent x-ray absorption and double reflection have been done by Templeton and Templeton near the $V K$ edge in crystalline $\text{VO}(\text{C}_5\text{H}_7\text{O}_2)_2$ [97]. The anisotropic feature was also observed in the diffraction experiments in Sodium Uranyl acetate, $\text{NaUO}_2(\text{O}_2\text{CCH}_3)_3$, and was found to be dramatically enhanced when the incident x-ray energy is tuned around $U L$ edge [98]. They have measured the polarization dependence of the diffraction intensity

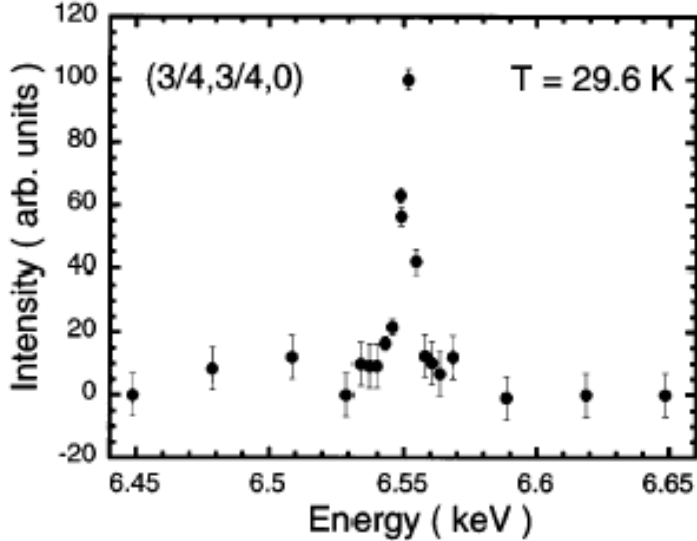


Figure 4. Energy dependence of the scattering intensity in $\text{La}_{1.5}\text{Sr}_{0.5}\text{MnO}_4$ at the orbital superlattice reflection $(3/4\ 3/4\ 0)$ [89].

as a function of the x-ray energy and derived the tensor elements of the x-ray scattering factors. The crystal structure of this compound is cubic and does not exhibit dichroism and birefringence on a macroscopic scale. Therefore, this is caused by a lack of the cubic symmetry around U ion which is located on threefold axes. With these works as a start, a number of experimental and theoretical studies about x-ray dichroism and birefringence have been performed [99, 100, 101, 102, 103, 104, 105, 106, 107, 108]. In particular, Dmitrienko developed this issue theoretically from the view point of the forbidden reflection [102, 103]. He expressed the x-ray scattering factor by the anisotropic x-ray susceptibility tensor and derived new extinction rules being valid near the absorption edge. This reflection is termed the anisotropy of tensor of susceptibility (ATS) reflection. In the microscopic point of view, these phenomena are attributed to the chemical bonding of the edge atom in an anisotropic chemical environment. This brings about the orientation of unoccupied electronic levels.

2.2. A variety of recent RXS experiments

In 1998, the resonant x-ray scattering was first applied to study of the orbital ordering in one of the manganites $\text{La}_{0.5}\text{Sr}_{1.5}\text{MnO}_4$ [89]. The formal valence of a Mn ion in this compound is 3.5+, that is, an average number of the e_g electron is 0.5 per ion. Before the RXS experiment, an alternating charge ordering with a $\sqrt{2}a \times \sqrt{2}a \times c$ unit cell was suggested by the electron diffraction experiments below 270K [109, 110]. In addition, the magnetically ordered structure with a $2\sqrt{2}a \times 2\sqrt{2}a \times 2c$ unit cell was observed below

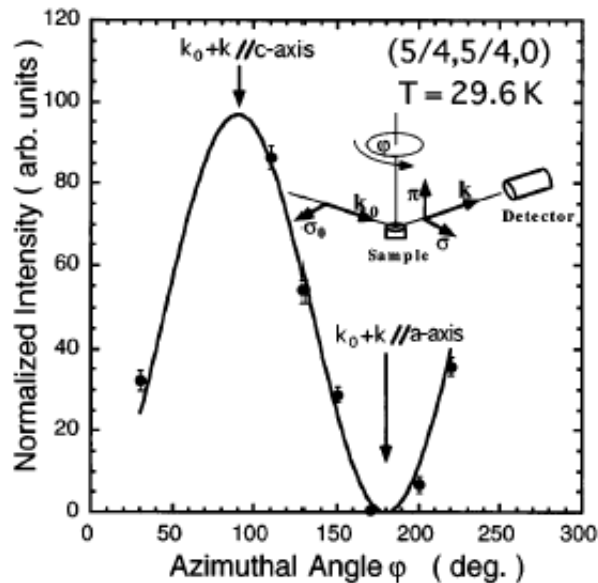


Figure 5. Azimuthal angle dependence of the scattering intensity in $\text{La}_{0.5}\text{Sr}_{1.5}\text{MnO}_4$ at the orbital superlattice reflection $(5/4, 5/4, 0)$ [89].

110K [111]. This is the so-called *CE*-type AF ordering associated with the charge ordering and has been already observed in manganites with pseudo-cubic perovskite structure. More than forty years ago, in order to explain the *CE*-type AF ordering observed in $\text{La}_{0.5}\text{Ca}_{0.5}\text{MnO}_3$, an alternate ordering of the chemical bonds between Mn and O ions, termed the covalent-bond ordering, was proposed [26, 30]. Through the systematic structural and magnetic studies by x-ray and neutron scatterings, this idea was reinforced, and the ordering of e_g orbital associated with distorted MnO_6 octahedra was supposed [38]. Therefore, it was expected in $\text{La}_{0.5}\text{Sr}_{1.5}\text{MnO}_4$ that the similar multi-component ordering is realized, although there was no direct evidence of the orbital ordering.

Murakami and coworkers applied RXS to investigate charge and orbital orderings in $\text{La}_{0.5}\text{Sr}_{1.5}\text{MnO}_4$ [89]. They utilized the following characteristics in this compound and RXS technique: (1) The expected orbital ordering has a unit cell with $\sqrt{2}a \times 2\sqrt{2}a \times c$ which is distinct from the unit cells for the spin and charge orderings. A schematic picture of the charge and orbital ordered state is shown in Fig. 3. (2) ASF in RXS is a tensor with respect to polarization of x ray. This is available to detect the asphericity of the electron density. (3) A magnitude of ASF in RXS is sensitive to a valence of ion. To detect the orbital ordering, the incident x-ray energy was tuned near the Mn *K* edge of 6.552KeV and the reflection at $(\frac{2l+1}{4}, \frac{2l+1}{4}, n)$ was chosen. This reflection corresponds to a unit cell of the orbital ordering and termed orbital superlattice reflection. The

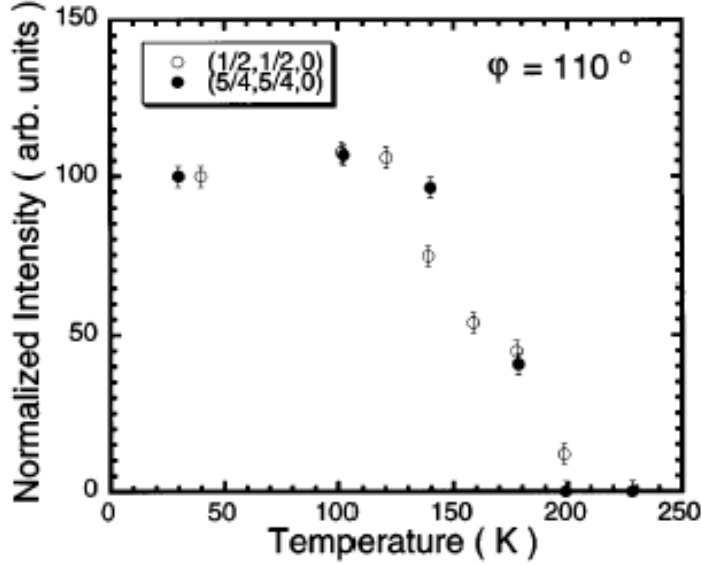


Figure 6. Temperature dependence of the scattering intensity in $\text{La}_{1.5}\text{Sr}_{0.5}\text{MnO}_4$ at the orbital superlattice reflection $(5/4\ 5/4\ 0)$ and that at the charge superlattice reflection $(1/2\ 1/2\ 0)$ [89].

structure factor at this point is represented by

$$F\left(\frac{2l+1}{4}\ \frac{2l+1}{4}\ 0\right) = f(\text{Mn}^{3+}(\text{A})) - f(\text{Mn}^{3+}(\text{B})), \quad (1)$$

where $f(\text{Mn}^{3+}(\text{A}))$ and $f(\text{Mn}^{3+}(\text{B}))$ are ASF's in Mn^{3+} with orbitals A and B, respectively. When all Mn^{3+} ions are equivalent, this reflection disappears due to the structure factor. This is the extinction rule in the x ray scattering. The experimental results of the incident x-ray energy dependence of the scattering intensity are presented in Fig. 4. The scattering intensity resonantly appears near the K -absorption edge, that is, the extinction rule is broken near the edge. This forbidden reflection is not ascribed to the normal part of ASF, unlike the well known case of the $(2l + 1\ 2m + 1\ 2n + 1)$ and $(2l\ 2m\ 2n)$ reflections in Ge due to the anharmonic lattice vibration, because of the following two reasons; (1) The scattering intensity shows a resonant behavior near the absorption edge. (2) The normal part of ASF is given by

$$f_{0A(B)}(\vec{K}) \propto \int e^{i\vec{K}\cdot\vec{r}} \rho_{A(B)}(\vec{r}), \quad (2)$$

where $f_{0A(B)}(\vec{K})$ is the normal part of ASF in a Mn^{3+} ion with A(B) orbital and $\rho_{A(B)}(\vec{r})$ is its charge distribution. Because of the symmetry of the charge distribution as

$$\rho_A(x, y, z) = \rho_B(y, x, z), \quad (3)$$

a difference of the normal part $f_{0A}(\vec{K}) - f_{0B}(\vec{K})$ vanishes at $\vec{K} = \left(\frac{2l+1}{4}\ \frac{2l+1}{4}\ 0\right)$.

The measurement of the angular dependence around the scattering vector, termed the azimuthal angle dependence, was utilized to confirm that this scattering results

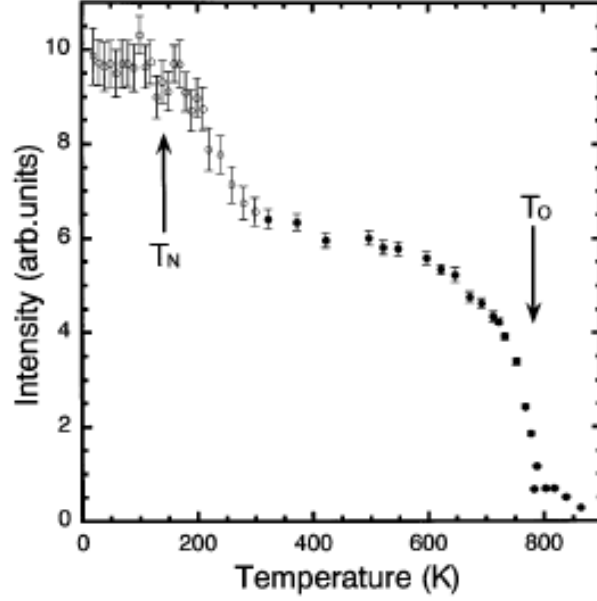


Figure 7. Temperature dependence of the scattering intensity in LaMnO₃ at the orbital superlattice reflection (3 0 0) [112].

from the anomalous part of ASF. The x-ray polarization coming from the synchrotron light source is highly polarized, such as the σ polarization in this case. Thus, the relative direction of electric vector to a sample is changed by rotating a sample around the scattering vector. The scattering due to the normal part of ASF does not show this dependence, since the ASF is scalar. The experimental results are shown in Fig. 5. The scattering intensity oscillates as a function of the azimuthal angle φ ; the intensity becomes its maximum (minimum) at $\varphi = 90^\circ$ (180°) where the incident x-ray polarization is parallel to the ab plane (c axis) of the sample. This dependence was fitted by a function $\sin^2 \varphi$ derived from the phenomenological calculation assuming the orbital ordering. Therefore, the forbidden reflections ascribed to the multiple scattering, such as the Ranninger scattering, is ruled out. It was concluded that the observed reflection originates from the anisotropic character of the anomalous part of ASF. The authors also measured the reflection at $(\frac{2l+1}{2} \frac{2l+1}{2} 0)$ being proportional to the difference between ASF's of Mn³⁺ and Mn⁴⁺:

$$F(\frac{2l+1}{2} \frac{2l+1}{2} 0) = f(\text{Mn}^{3+}(\text{A})) + f(\text{Mn}^{3+}(\text{B})) - 2f(\text{Mn}^{4+}) + c, \quad (4)$$

with ASF of Mn⁴⁺ $f(\text{Mn}^{4+})$ and a constant c . Both the reflections at $(\frac{2l+1}{4} \frac{2l+1}{4} 0)$ and $(\frac{2l+1}{2} \frac{2l+1}{2} 0)$ appear around 200K and show almost identical temperature dependence as shown in Fig. 6. This implies that the charge and orbital order parameters couple with each other.

After the first observation, this technique was applied to a parent compound of

Table 1. A list of experimental studies of RXS

Materials	References
LaMnO ₃	[112, 121]
La _{1-x} Sr _x MnO ₃ ($x=0.08, 0.1, 0.11, 0.12$)	[116, 118, 125]
Nd _{0.5} Sr _{0.5} MnO ₃	[127]
Pr _{1-x} Ca _x MnO ₃ ($x=0.25, 0.4, 0.5$)	[117, 121, 122]
La _{2-x} Sr _x MnO ₄ ($0.4 < x < 0.5$)	[89, 123]
LaSr ₂ Mn ₂ O ₇	[119, 120]
La _{1-x} Sr _x MnO ₃ (Artificial Lattice)	[124]
YTiO ₃	[128]
LaTiO ₃	[126]
YVO ₃	[127]
V ₂ O ₃	[114]
DyB ₂ C ₂	[129, 130, 133]
CeB ₆	[132]
UPd ₃	[131]

CMR manganites LaMnO₃ [112]. As introduced in Sec. 1, an alternate ordering of orbital with a $\sqrt{2}a \times \sqrt{2}a \times 2c$ unit cell is expected from the largely distorted MnO₆ octahedron and the *A*-type AF ordering. The resonant behavior near the Mn *K*-absorption edge was observed at (300) corresponding to the orbital superlattice reflection point. The $\sin^2 \varphi$ -type azimuthal angle dependence was confirmed only at the experimental arrangement where the scattered x-ray polarization λ_f is π . On the contrary, the intensity almost disappears in the case of $\lambda_f = \sigma$. This is consistent with the symmetry of the aspherical charge cloud shown in Fig. 2. The observed temperature dependence of the RXS intensity is shown in Fig. 7. The intensity rapidly increases at 780K which coincides with the structural phase transition temperature from the pseudo-cubic perovskite structure (*O** phase) to the orthorhombic one (*O'* phase).

At the same time, independently of perovskite manganites, RXS was applied to V₂O₃ [113, 114] and was studied theoretically and experimentally as a probe to detect the orbital ordering. Nowadays, RXS has been widely utilized to study of the orbital degree of freedom in several manganites [115, 116, 117, 118, 119, 120, 121, 122, 123, 124, 125], other transition-metal oxides [126, 127, 128] and *f*-electron systems [129, 130, 131, 132, 133]. Simultaneously, theories of RXS in the several view points were developed [134, 135, 136, 137, 138, 139, 140, 141, 142, 143, 144, 145, 146, 147, 148, 149, 150]. This technique is also applied to detect the charge ordering in transition-metal oxides [89, 117, 120, 151, 152, 153]. The published experimental RXS studies for the orbital states are listed in table 1.

In particular, the following two experiments provided key information for the mechanism of RXS and orbital ordering in manganites. (1) *La*_{1-*x*}*Sr*_{*x*}*MnO*₃ at $x \sim 1/8$

T	$T_{OO}=145\text{K}$ $T_C=172\text{K}$ $T_H=291\text{K}$		
Spin	Ferromagnetic		Paramagnetic
Charge	Insulating	Metallic	Insulating
Lattice	Triclinic (Pseudo-cubic)	Monoclinic (JT distorted)	Orthorhombic (O^*)
Orbital	Order	Disorder	

Figure 8. The spin, charge, lattice and orbital phase diagram in $\text{La}_{0.88}\text{Sr}_{0.12}\text{MnO}_3$.

[116, 118]: By doping of holes into LaMnO_3 , the magnetic, electric and structural properties rapidly change and a number of phase boundaries are entangled around $x = 1/8$. In $\text{La}_{0.88}\text{Sr}_{0.12}\text{MnO}_3$, the electric resistivity shows metallic behavior below the ferromagnetic transition temperature $T_C = 172\text{K}$ and shows sharp upturn below a temperature $T_{OO} = 145\text{K}$ [6, 154]. Successive structural-phase transitions were observed by neutron and x-ray scattering experiments: the orthorhombic phase (O^* phase) to the monoclinic one (M phase) at $T_H = 291\text{K}$ and the M phase to the triclinic one (T phase) at T_{OO} [155]. The Jahn-Teller type lattice distortion in MnO_6 octahedra, which is a similar type in LaMnO_3 , is confirmed below T_H but dramatically weakens at T_{OO} [156, 157, 116]. The phase diagram in $\text{La}_{0.88}\text{Sr}_{0.12}\text{MnO}_3$ is summarized in Fig. 8 and the temperature dependence of lattice parameter observed by the neutron scattering is presented in Fig. 9 [116]. RXS experiments was carried out and the scattering intensity was observed at (030) below T_{OO} as shown in Fig. 10. This is quite surprising results, since the orbital order appears in the T phase where the Jahn-Teller type lattice distortion is almost quenched. This experimental result implies that (i) the present orbital ordering is not caused by the cooperative Jahn-Teller effects, and (ii) RXS in this phase does not originate from the lattice distortion in MnO_6 octahedra. The theoretical model by taking into account the orbital order well explains several anomalous experiments: the magnetic field dependence of T_{OO} and the enhancement of the magnetization at T_{OO} [116, 76, 158]. Through the recent systematic studies of $\text{La}_{1-x}\text{Sr}_x\text{MnO}_3$ with a wide range of x around $1/8$, it was found that there exists a vertical phase boundary at $x_c \sim 0.11$ [159]. Below x_c , the orbital order and the Jahn-Teller type lattice distortion simultaneously appear at the structural phase transition from the O^* to O' phases. (2) $\text{Pr}_{0.6}\text{Ca}_{0.4}\text{MnO}_3$ [117, 121]: From the structural, magnetic and transport experiments, it was revealed that the charge and orbital ordered state appears in $\text{Pr}_{1-x}\text{Ca}_x\text{MnO}_3$ with $0.3 < x < 0.5$ [160]. The unit cells for these orderings are the same as those in $\text{La}_{0.5}\text{Ca}_{0.5}\text{MnO}_3$, although an excess carrier $\delta x = |x - 0.5|$ may weaken the orderings. RXS experiments were carried out in $x=0.4$ and 0.5 , and

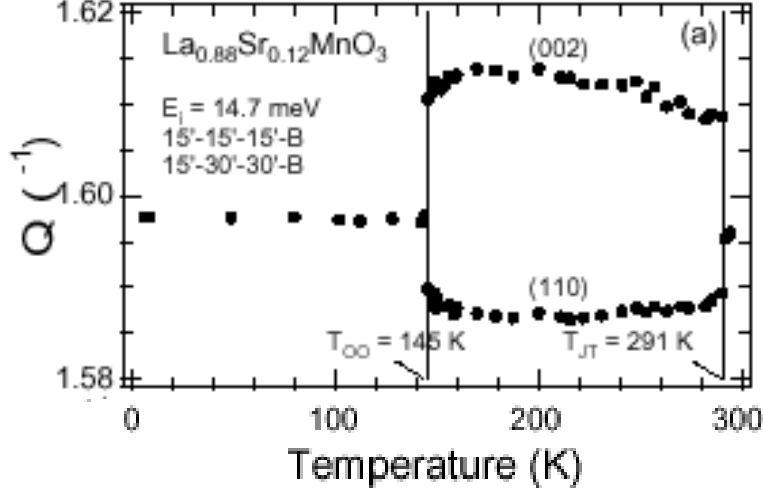


Figure 9. Temperature dependence of lattice parameter in $\text{La}_{0.88}\text{Sr}_{0.12}\text{MnO}_3$ [116].

the reflections at $(0\ 2n+1\ 0)$ (charge superlattice reflection) and at $(0\ \frac{2n+1}{2}\ 0)$ (orbital superlattice reflection) were observed below 245K. In particular, the peak widths of both the scatterings were examined in detail, and the following characteristics were found out (see Fig. 11): (i) At low temperatures, the half of width for the half maxima (HWHM) of the orbital superlattice peak does not reach the experimental resolution limit, in contrast to the charge superlattice peak, and (ii) with decreasing temperature above 245K, HWHM of the charge superlattice peak is more rapidly reduced than that of the orbital one. As mentioned later (Sec. 3.4), RXS at the orbital superlattice reflection detects the ordering of the x -component of the pseudo-spin operator T_x which represents the tetragonal component of an electronic cloud. The above experiments suggest that the charge order fluctuation is more correlated than that of T_x above the ordering temperature and no long range order of T_x occurs in this compound.

3. Theoretical framework

3.1. Scattering cross section

The differential scattering cross section of x ray from electrons in solid is formulated by perturbational calculation in terms of the interactions between electrons and photons. We start with the Hamiltonian for the electron-photon coupled system:

$$\mathcal{H} = \mathcal{H}_e + \mathcal{H}_p + \mathcal{H}_{e-p}, \quad (5)$$

where the Hamiltonian for the electronic system \mathcal{H}_e , that for photons \mathcal{H}_p and the interactions between the two \mathcal{H}_{e-p} . \mathcal{H}_{e-p} is divided into the two terms for the interactions between the electronic current $\vec{j}(\vec{r})$ and the vector potential $\vec{A}(\vec{r})$, and the electronic charge $\rho(\vec{r})$ and $\vec{A}(\vec{r})$ as follows,

$$\mathcal{H}_{e-p} = \mathcal{H}_j + \mathcal{H}_\rho$$

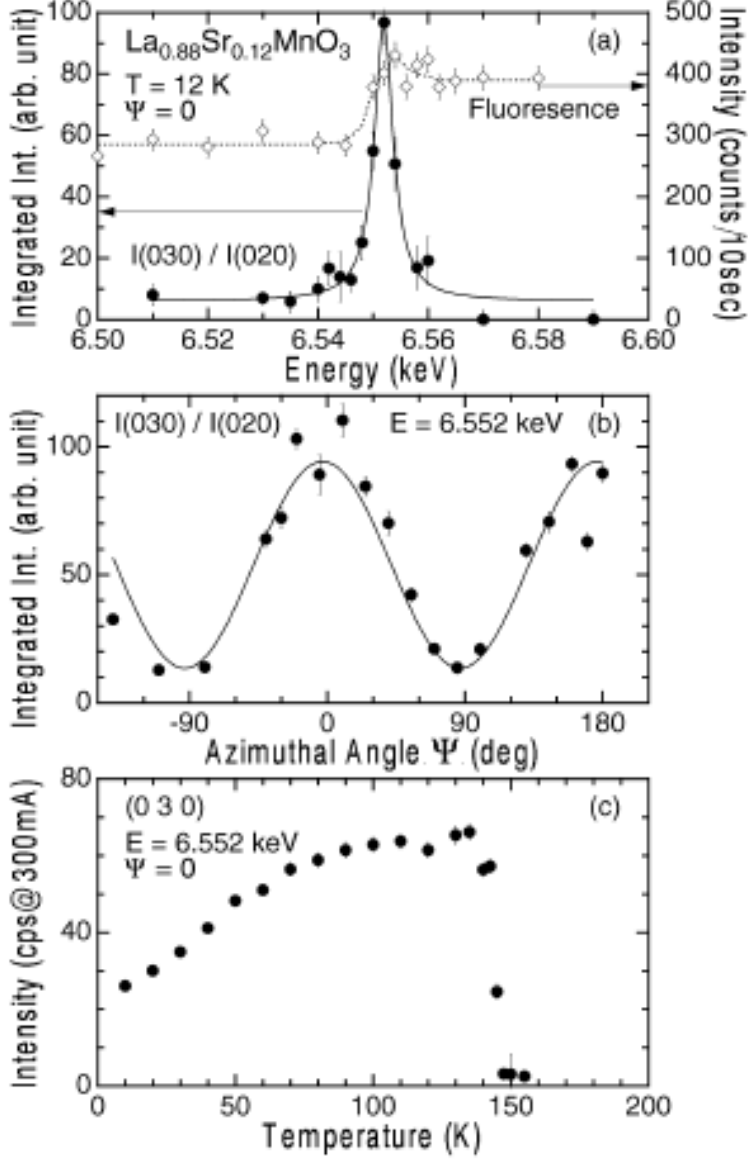


Figure 10. (a) Energy dependence of RXS intensity of the orbital superlattice reflection (0 3 0) in $\text{La}_{0.88}\text{Sr}_{0.12}\text{MnO}_3$. The dashed curve represents fluorescence. (b) The azimuthal angle dependence of the (0 3 0) reflection. The solid curve is the two fold squared sine curve of angular dependence. (c) Temperature dependence of the (0 3 0) peak intensity [116].

$$= -\frac{e}{c} \int d\vec{r} \vec{j}(\vec{r}) \cdot \vec{A}(\vec{r}) + \frac{e^2}{2mc^2} \int d\vec{r} \rho(\vec{r}) \vec{A}(\vec{r})^2. \quad (6)$$

We assume that both \mathcal{H}_e and \mathcal{H}_p are diagonal. The S -matrix in the second order terms with respect to $\vec{A}(\vec{r})$ provides the differential scattering-cross section of x ray

CON

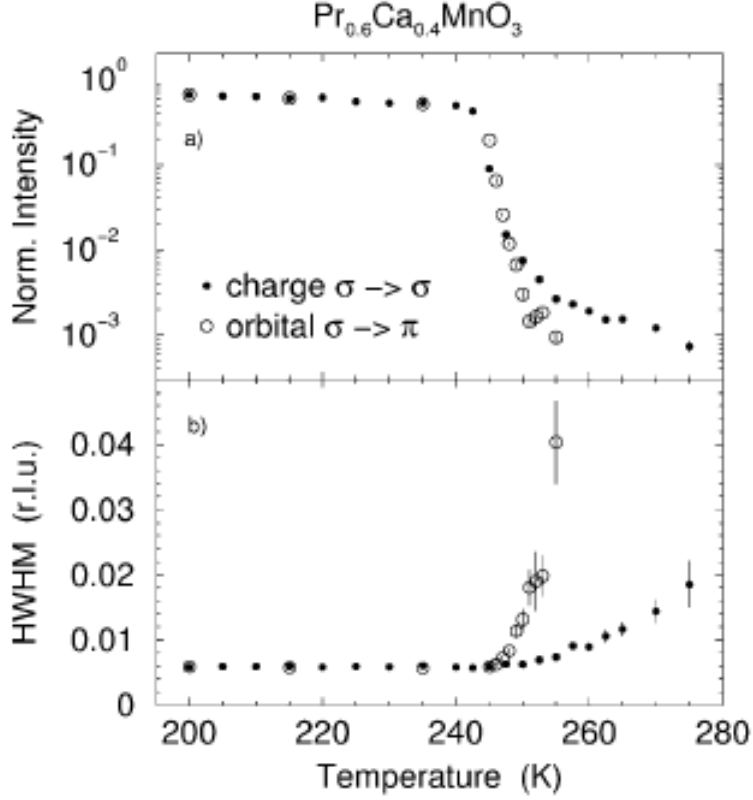


Figure 11. (a) Temperature dependence of the peak intensities of the (0 3 0) charge superlattice reflection (closed circles) and the (0 2.5 0) orbital superlattice reflection (open circles) in $\text{Pr}_{0.6}\text{Ca}_{0.4}\text{MnO}_3$. (b) Temperature dependence of the half widths at half maximum [117].

[161, 162, 163]:

$$\begin{aligned} \frac{d^2\sigma}{d\Omega d\omega_f} &= \sigma_T \frac{\omega_f}{\omega_i} \sum_f \left| S_1 \vec{e}_{k_i \lambda_f} \cdot \vec{e}_{k_f \lambda_f} + \sum_{\alpha\beta} (\vec{e}_{k_i \lambda_i})_\alpha S_{2\alpha\beta} (\vec{e}_{k_f \lambda_f})_\beta \right|^2 \\ &\times \delta(\varepsilon_f + \omega_f - \varepsilon_i - \omega_i), \end{aligned} \quad (7)$$

where

$$S_1 = \langle f | \rho(\vec{k}_i - \vec{k}_f) | i \rangle, \quad (8)$$

and

$$\begin{aligned} S_{2\alpha\beta} &= \frac{m}{e^2} \sum_m \left(\frac{\langle f | \vec{j}(-\vec{k}_i)_\alpha | m \rangle \langle m | \vec{j}(\vec{k}_f)_\beta | i \rangle}{\varepsilon_i - \varepsilon_m - \omega_f + i\eta} \right. \\ &\quad \left. + \frac{\langle f | \vec{j}(\vec{k}_f)_\beta | m \rangle \langle m | \vec{j}(-\vec{k}_i)_\alpha | i \rangle}{\varepsilon_i - \varepsilon_m + \omega_i + i\eta} \right). \end{aligned} \quad (9)$$

This is the so-called Kramers-Heisenberg formula. We consider the scattering of x ray with momentum \vec{k}_i , energy $\omega_i = c|\vec{k}_i|$ and polarization λ_i , to \vec{k}_f , ω_f and λ_f . $\vec{e}_{k_i \lambda_i}$

($l = i, f$) is the polarization vector of x ray, and $|i\rangle$, $|m\rangle$ and $|f\rangle$ indicate the electronic states in the initial, intermediate and final scattering states with energies ε_i , ε_m and ε_f , respectively. A factor:

$$\sigma_T = \left(\frac{e^2}{mc^2} \right)^2, \quad (10)$$

is the total scattering cross section of the Thomson scattering and η in the denominator in S_2 is an infinitesimal positive constant. $\vec{j}(\vec{k})$ and $\rho(\vec{k})$ are defined by the Fourier transforms of $\rho(\vec{r})$ and $\vec{j}(\vec{r})$:

$$\rho(\vec{k}) = \int d\vec{r} \rho(\vec{r}) e^{-i\vec{k}\cdot\vec{r}}, \quad (11)$$

and

$$\vec{j}(\vec{k}) = \int d\vec{r} \vec{j}(\vec{r}) e^{-i\vec{k}\cdot\vec{r}}, \quad (12)$$

respectively. In the elastic scattering, $\rho(\vec{k})$ and $\vec{j}(\vec{k})$ are decomposed into the charge and current operators defined at each lattice site:

$$\rho(\vec{k}) = \sum_l \rho_l(\vec{k}) e^{-i\vec{k}\cdot\vec{r}_l}, \quad (13)$$

and

$$\vec{j}(\vec{k}) = \sum_l \vec{j}_l(\vec{k}) e^{-i\vec{k}\cdot\vec{r}_l}. \quad (14)$$

Then, we define the atomic scattering factor (ASF) at site l :

$$f_{l\alpha\beta}(\vec{k}_i, \vec{k}_f) = f_{0l}(\vec{k}_i, \vec{k}_f) \delta_{\alpha\beta} + \Delta f_{l\alpha\beta}(\vec{k}_i, \vec{k}_f), \quad (15)$$

where the first and second terms are called the normal and anomalous terms of ASF, respectively. These are derived from S_1 and $S_{2\alpha\beta}$ in Eqs. (8) and (9) where $\rho(\vec{k})$ and $\vec{j}(\vec{k})$ are replaced by $\rho_l(\vec{k})$ and $\vec{j}_l(\vec{k})$, respectively.

When the incident x-ray energy ω_i is far from the energy difference of the initial and intermediate electronic states $\Delta\varepsilon_{mi} = \varepsilon_m - \varepsilon_i$, S_1 dominates the scattering. On the other hand, when ω_i is close to $\Delta\varepsilon_{mi}$, the real part of the denominator in the second term of S_2 becomes zero and the scattering intensity from this term increases divergently. This is the resonant x-ray scattering. Here, a life time of the intermediate electronic state $|m\rangle$ limits the scattering intensity to a finite value [161]. This life time arises from the mixing of $|m\rangle$ and other electronic states, such as $|i\rangle$ and $|f\rangle$. This is not included in \mathcal{H}_e in Eq.(5), because it is assumed to be diagonal. Electron correlation effects on a core hole and/or an excited electron by x ray cause this effect which is represented by the self energy Σ . The denominator of the second term in S_2 is replaced by $\varepsilon_i - \varepsilon_m + \omega_i + i\Gamma$ where $\text{Re}\Sigma$ is included in the definition of ε_m and $\text{Im}\Sigma + \eta$ is denoted by Γ . It is known that a magnitude of Δf at the resonant condition is comparable to that of f_0 [98, 99].

Here we consider that, in the intermediate scattering states, one electron is excited from orbital a to orbital b at a same site [134]. The current operator $\vec{j}(\vec{k})$ in Eq. (12) is represented by

$$\vec{j}(\vec{k}) = -\frac{ie}{2m} \sum_{i\sigma} e^{i\vec{k}\cdot\vec{r}_i} \vec{A}_{ab}(\vec{k}) c_{ia\sigma}^\dagger c_{ib\sigma} + H.c., \quad (16)$$

with

$$\vec{A}_{ab}(\vec{k}) = \int d\vec{r} e^{-i\vec{k}\cdot\vec{r}} \{ \phi_a^*(\vec{r}) \vec{\nabla} \phi_b(\vec{r}) - \vec{\nabla} \phi_a^*(\vec{r}) \phi_b(\vec{r}) \}. \quad (17)$$

$c_{ia(b)\sigma}$ is the annihilation operator of an electron with orbital $a(b)$ and spin σ at site i , and $\phi_{a(b)}(\vec{r})$ is the Wannier function for an electron in the orbital $a(b)$. \vec{r}_i indicates the position of the i -th ion in a crystal lattice. Consider the case of the resonant scattering where ω_i is tuned at the K edge of a transition-metal ion and b in Eqs. (16) and (17) indicates the $1s$ orbital in this ion. In a crystal with inversion symmetry, the multipole expansion is valid. Note that a relevant region of the integral in Eq. (17) is determined by the average atomic radius $\langle r_{1s} \rangle$ of the $1s$ orbital which is much smaller than the wave length λ of x ray. In the case of a Mn ion, the ratio $\lambda/\langle r_{1s} \rangle$ is about 1/100. Thus electric quadrupole transition is much smaller than the electric dipole one and the anomalous part of ASF, $\Delta f_{\alpha\beta}(\vec{k}_i, \vec{k}_f)$, in Eq. (15) is almost independent of the momentum of x ray, unlike the normal part of ASF, $f_0(\vec{k}_i, \vec{k}_f)$. In comparison with other experimental methods, RXS has the following advantages to detect the orbital ordering in transition-metal oxides: (1) The wave length of x ray, which is tuned near the K absorption edge of a transition-metal ion, is shorter than a lattice constant of the perovskite unit cell. Thus, the diffraction experiments can be carried out for the orbital superlattice, unlike Raman scattering and optical reflection/absorption experiments. (2) As shown in Eq. (9), S_2 is a tensor with respect to the incident and scattered x-ray polarizations. On the contrary, S_1 is a scalar. (3) By tuning the x-ray energy at the absorption edge, the scattering from a specific element, such as a Mn ion, can be identified.

3.2. Microscopic mechanism of RXS in orbital ordered states

One of the main issues in RXS as a probe to detect the orbital ordering is its microscopic mechanism of the scattering in orbital ordered state, i.e. the mechanism of the anisotropic tensor elements of ASF. Let us consider the RXS experiments applied to the orbital ordered $3d$ transition-metal oxides. The initial x ray tuned around the K edge of the transition-metal ion causes the dipole transition from the $1s$ orbital to the $4p$ orbital in the intermediate scattering states. Thus, this transition itself does not access to the $3d$ orbital directly where the orbital ordering occurs, and some mechanisms which bring about the anisotropy of ASF are required. The similar situation occurs in RXS applied to the quadrupolar ordering in $4f$ electron systems. Here, x-ray energy is tuned around the L edge of $4f$ rare-earth ions and the $2p - 5d$ transition is brought about. Although some methods can access directly to the orbital concerned [131, 147, 148], these experiments are limited as discussed later. This is because the wave length of x ray should satisfy both the resonant and diffraction conditions. In this section, we introduce the microscopic mechanisms of RXS in orbital ordered manganites.

One of the promising candidates, which bring about the anisotropy of ASF, is the Coulomb interaction between $3d$ and $4p$ electrons [134]. Consider an orbital ordered state in perovskite manganites. There exists the Coulomb interaction between $3d$ and

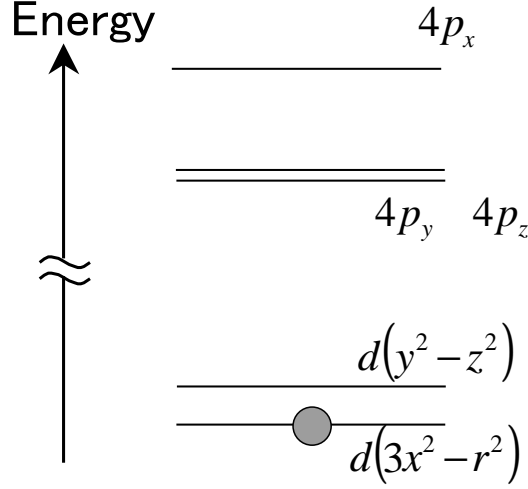


Figure 12. A schematic energy diagram of the Mn $4p$ orbitals at the $d_{3x^2-r^2}$ orbital occupied site in the Coulomb mechanism.

$4p$ electrons represented by

$$\mathcal{H}_{3d-4p} = \sum_{\gamma\gamma'\alpha\sigma\sigma'} V_{\gamma\gamma'\alpha} d_{\gamma\sigma}^\dagger d_{\gamma'\sigma} P_{\alpha\sigma'}^\dagger P_{\alpha\sigma}, \quad (18)$$

where $d_{\gamma\sigma}$ is the annihilation operator of the $3d$ electron with orbital $\gamma (= 3z^2 - r^2, x^2 - y^2)$ and spin $\sigma (= \uparrow, \downarrow)$, and $P_{\alpha\sigma}$ is the annihilation one of the $4p$ electron with the Cartesian coordinate $\alpha (= x, y, z)$. The Coulomb interaction $V_{\gamma\gamma'\alpha}$ between the two is given by

$$V_{\gamma\gamma'\alpha} = \begin{cases} F_0(3d, 4p) + \frac{4}{35} F_2(3d, 4p) \cos(\theta_\gamma - \frac{2\pi}{3} m_\alpha) & \text{for } \gamma' = \gamma \\ \frac{4}{35} F_2(3d, 4p) \sin(\theta_\gamma - \frac{2\pi}{3} m_\alpha) & \text{for } \gamma' = -\gamma \end{cases}, \quad (19)$$

where $(m_x, m_y, m_z) = (1, 2, 3)$, $-\gamma$ indicates a counterpart of γ , and $F_{0(2)}(3d, 4p)$ is the Slater-integral between $3d$ and $4p$ electrons. θ_γ characterizes the wave function of the occupied orbital as $|d_\gamma\rangle = \cos(\theta_\gamma/2)|d_{3z^2-r^2}\rangle - \sin(\theta_\gamma/2)|d_{x^2-y^2}\rangle$. Due to this interaction, the three $4p$ orbitals split and the energy levels of the $4p_y$ and $4p_z$ orbitals relatively decrease at the site where the $d_{3x^2-r^2}$ orbital is occupied (see Fig. 12). As a result, the anisotropy of ASF is brought about such that $|\Delta f_{lyy}| = |\Delta f_{lzz}| \equiv f_s$, $|\Delta f_{lxx}| \equiv f_l$ and $f_l < f_s$. At a site where $d_{3y^2-r^2}$ orbital is occupied, the conditions $|\Delta f_{lxx}| = |\Delta f_{lzz}| \equiv f_s$ and $|\Delta f_{lyy}| \equiv f_l$ is derived. A RXS intensity at the orbital superlattice reflection point is proportional to $|\Delta f_{3x^2-r^2\alpha\alpha} - \Delta f_{3y^2-r^2\alpha\alpha}|^2$ and is finite in the cases of $\alpha = x$ and y . These are consistent with the experimental results in the azimuthal angle dependence of the scattering intensity. In addition to the $3d-4p$ Coulomb interaction, the inter-site Coulomb interaction between Mn $3d$ and O $2p$ electrons brings about the anisotropy of ASF. Because there exists a strong hybridization between Mn $3d$ and O $2p$ orbitals, the $|d_{3x^2-r^2}^1\rangle$ state strongly mixes with the $|d_{3x^2-r^2}^1 d_{y^2-z^2}^1 \underline{L}_{y^2-z^2}\rangle$ state. $\underline{L}_{y^2-z^2}$ indicates

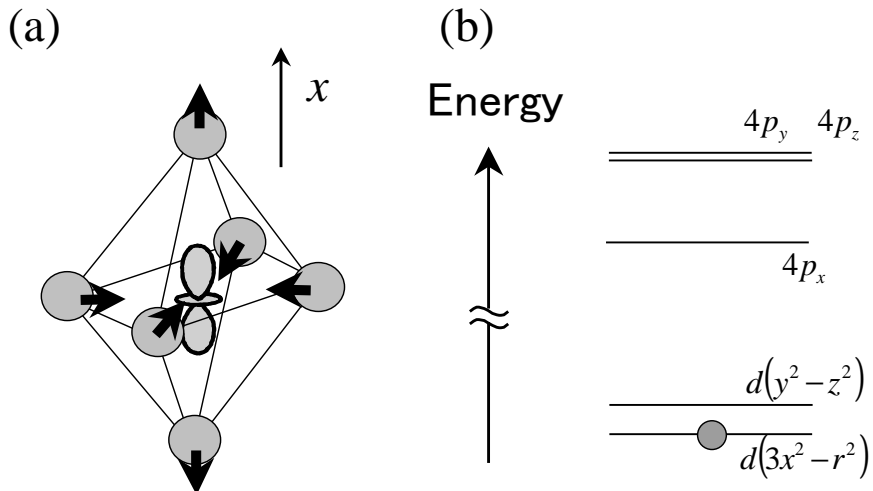


Figure 13. (a) A distortion in a MnO_6 octahedron where $d_{3x^2-r^2}$ orbital is occupied by an electron. (b) A schematic energy diagram of the Mn $4p$ orbitals at the $d_{3x^2-r^2}$ orbital occupied site in the Jahn-Teller mechanism.

a state where one hole occupies the linear combination of the ligand O $2p$ orbitals with the $y^2 - z^2$ symmetry. This interaction is given by

$$\mathcal{H}_{2p-4p} = \sum_{\gamma\alpha\sigma\sigma'} V_{\gamma\alpha}^{inter} p_{\gamma\sigma}^{(h)\dagger} p_{\gamma\sigma}^{(h)} P_{\alpha\sigma'}^\dagger P_{\alpha\sigma'}, \quad (20)$$

with

$$V_{\gamma\alpha}^{inter} = -\varepsilon - \frac{\varepsilon\rho^2}{5} \cos(\theta_\gamma + m_\alpha \frac{2\pi}{3}), \quad (21)$$

where $p_{\gamma\sigma}^{(h)}$ is the annihilation operator of the $2p$ hole. $\varepsilon = Ze^2/a$ and $\rho = \langle r_{4p} \rangle/a$ with $Z = 2$ and the average radius of the Mn $4p$ orbital $\langle r_{4p} \rangle$. The relative level structure caused by this interaction is the same with that shown in Fig. 12. The two mechanisms cause the anisotropy of ASF cooperatively and are termed the Coulomb mechanism. ASF based on this mechanism were calculated in a MnO_6 cluster at first (Refs. [134, 135]). Then, the theory was developed through the calculations where the itinerant character of the $4p$ electrons is introduced (Refs. [136, 138]). These results are reviewed in more detail later.

Another mechanism of the anisotropy of ASF was proposed from the view point of the Jahn-Teller type lattice distortion [140, 141, 142]. Consider the $d_{3x^2-r^2}$ orbital occupied site. A lattice distortion of an O_6 octahedron along the x direction is often observed around this Mn site (Fig. 13 (a)). This is termed the Jahn-Teller type lattice distortion. Since the Mn-O bond lengths along the x directions are elongated, the hybridization between O $2p_x$ and Mn $4p_x$ orbitals in these bonds is weaker than others. As a result, the three $4p$ orbitals split so that the energy level of the $4p_x$ orbital is lower than those of the $4p_y$ and $4p_z$ orbitals (see Fig. 13(b)), because the $4p$ orbitals

are the so-called anti-bonding orbitals. This tendency is opposite to that due to the Coulomb mechanism and is termed the Jahn-Teller mechanism. The anisotropy of ASF at the K edge is given such that $|\Delta f_{l_{yy}}| = |\Delta f_{l_{zz}}| \equiv f_s$, $|\Delta f_{l_{xx}}| \equiv f_l$ and $f_l > f_s$. This scenario was demonstrated by the LSDA+U method (Ref. [140]) and the LDA method in the KKR scheme (Ref. [142]). The linear muffin-tin orbital (LMTO) method was utilized to calculate the local density of states (DOS) for the $4p$ electrons in the crystal structure of LaMnO_3 . The calculated anisotropy of DOS was compared with the x-ray absorption and RXS spectra. ASF based on this mechanism was also calculated by the finite difference method and the multiple scattering theory in a finite cluster system (Ref. [141]). Here the effects of the core hole potential are introduced unlike the band structure calculations. It is noted that the calculated spectra obtained by the two methods, i.e. the band calculations and the cluster calculations, show large differences with each other. This may be attributed to the itinerant effects of the $4p$ electrons and the core hole potential, which are treated properly in the former and the later, respectively.

As mentioned above, the RXS intensity is given by $|f_l - f_s|^2$. This is proportional to the square of the level splitting of the Mn $4p$ orbitals $\Delta (\equiv \varepsilon_x - \varepsilon_z)$, where $\varepsilon_{x(z)}$ is the energy level of the Mn $4p_{x(z)}$ orbital, and does not depend on the sign of Δ [112]. Then, quantitative estimations for the anisotropy of ASF are required. However, it is, in general, difficult theoretically to treat quantitatively both the local correlation effects, such as the core hole potential and the $3d$ - $4p$ Coulomb interactions, and the large itinerant character of the $4p$ electrons on an equal footing. Until now, there are not direct evidences and the dominant mechanism of the anisotropy of ASF is still controversial. The measurements of the interference of S_1 and S_2 in Eq. (7) may be available to determine the sign of Δ [135, 124]. On the other hand, the following experiments suggest that the Coulomb mechanism is expected to dominate in these compounds: (1) As introduced in Sect. 2.2, the neutron scattering experiments in $\text{La}_{0.88}\text{Sr}_{0.12}\text{MnO}_3$ show that the Jahn-Teller type lattice distortion exists among $291\text{K} > T > 145\text{K}$, and this distortion is almost quenched below 145K . On the other hand, RXS intensity is not observed in the region of $291\text{K} > T > 145\text{K}$ but appears below 145K [116, 118]. That is, the region where the Jahn-Teller distortion appears and that where the RXS intensity is observed are different. These results suggest that the anisotropy of ASF in this compound is not caused by the Jahn-Teller mechanism. (2) YTiO_3 is known to show the orbital ordered state where four kinds of orbitals are arranged in a unit cell. RXS experiments in YTiO_3 were recently carried out, in detail, at several orbital superlattice reflection points and the polarization configurations. Through the quantitative analyses, it was concluded that the relative scattering intensities can not be explained by ASF expected from the lattice distortion but is consistent with ASF in the Coulomb mechanism [128]. In order to clarify the mechanism of the anisotropy of ASF, the further experimental and theoretical researches are required.

By taking into account the above facts, we review, in the following, the calculations of ASF based on the Coulomb mechanism [138, 136]. Let us start with the model

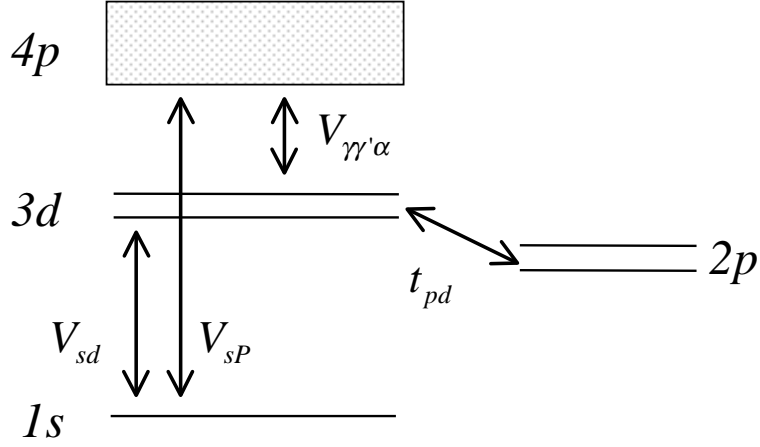


Figure 14. A schematic energy diagram for the Hamiltonian in Eq. (22).

Hamiltonian:

$$\mathcal{H} = \mathcal{H}_{\text{cluster}} + \mathcal{H}_{\text{band}}. \quad (22)$$

$\mathcal{H}_{\text{cluster}}$ describes the electronic system in a MnO_6 cluster where x ray is absorbed. Electrons in this cluster couple with the Mn 4p band given by $\mathcal{H}_{\text{band}}$. The Mn 3d, 4p and 1s orbitals and the O 2p ones are introduced in $\mathcal{H}_{\text{cluster}}$, and the corresponding annihilation operators are defined by $d_{l\gamma\sigma}$, $P_{l\alpha\sigma}$ $s_{l\sigma}$ and $p_{l\gamma\sigma}$, respectively, with orbital $\gamma(= 3z^2 - r^2, x^2 - y^2)$, spin $\sigma(=\uparrow, \downarrow)$ and Cartesian coordinate $\alpha(= x, y, z)$. The O 2p molecular orbitals are formed from linear combinations of the six O 2p orbitals in the octahedron. A simple cubic lattice of a Mn ion is considered in $\mathcal{H}_{\text{band}}$ and the Mn 4p orbitals are introduced at each Mn site. The explicit form of the Hamiltonian is given by

$$\mathcal{H}_{\text{cluster}} = \mathcal{H}_{3d} + \mathcal{H}_{3d-4p} + \mathcal{H}_{1s,4p} + \mathcal{H}_{1s-3d,4p} + \mathcal{H}_{2p-3d}, \quad (23)$$

with

$$\begin{aligned} \mathcal{H}_{3d} = & \varepsilon_d \sum_{\gamma\sigma} d_{l\gamma\sigma}^\dagger d_{l\gamma\sigma} + U \sum_{\gamma} n_{l\gamma\uparrow}^d n_{l\gamma\downarrow}^d + U' \sum_{\sigma\sigma'} n_{l\gamma\sigma}^d n_{l-\gamma\sigma'}^d \\ & + I \sum_{\sigma\sigma'} d_{l\gamma\sigma}^\dagger d_{l-\gamma\sigma'}^\dagger d_{l\gamma\sigma'} d_{l-\gamma\sigma} - J_H \vec{S}_l \cdot \vec{S}_{l'}, \end{aligned} \quad (24)$$

$$\mathcal{H}_{1s,4p} = \varepsilon_P \sum_{\alpha\sigma} P_{l\alpha\sigma}^\dagger P_{l\alpha\sigma} + \varepsilon_s \sum_{\sigma} s_{l\sigma}^\dagger s_{l\sigma}, \quad (25)$$

$$\mathcal{H}_{1s-3d,4p} = n_{hl} \left(\sum_{\gamma} V_{sd} n_{l\gamma}^d + \sum_{\alpha} V_{sP} n_{l\alpha}^P \right), \quad (26)$$

$$\mathcal{H}_{2p-3d} = \varepsilon_p \sum_{\gamma\sigma} p_{l\gamma\sigma}^\dagger p_{l\gamma\sigma} + t_{pd} \sum_{\gamma\sigma} (d_{l\gamma\sigma}^\dagger p_{l\gamma\sigma} + H.c.), \quad (27)$$

and

$$\mathcal{H}_{\text{band}} = \varepsilon_P \sum_{m \neq l\alpha\sigma} P_{m\alpha\sigma}^\dagger P_{m\alpha\sigma} + \sum_{j\delta\alpha\beta\sigma} t_\alpha^\beta P_{m\alpha\sigma}^\dagger P_{m+\delta\beta\alpha\sigma}. \quad (28)$$

\mathcal{H}_{3d-4p} in Eq. (23) is presented in Eq. (18), and a site where x ray is absorbed is denoted by l . A schematic energy level diagram is shown in Fig. 14. \mathcal{H}_{3d} is for the Mn 3d electronic system where U , U' and I are the intra-orbital Coulomb interaction, the inter-orbital one and the exchange interaction between e_g electrons, respectively, and J_H is the Hund coupling between e_g and t_{2g} spins. We define the number operator $n_{l\gamma}^d = \sum_\sigma n_{l\gamma\sigma}^d = \sum_\sigma d_{l\gamma\sigma}^\dagger d_{l\gamma\sigma}$ and the spin operator:

$$\vec{S}_l = \frac{1}{2} \sum_{\sigma_1\sigma_2\gamma} d_{l\gamma\sigma_1}^\dagger (\vec{\sigma})_{\sigma_1\sigma_2} d_{l\gamma\sigma_2}, \quad (29)$$

for the e_g electrons and the spin operator \vec{S}_{tl} for the t_{2g} electrons with $S = 3/2$. $\mathcal{H}_{1s-3d,4p}$ describes the core hole potential between a 1s hole $n_l^h (= 2 - \sum_\sigma s_{l\sigma}^\dagger s_{l\sigma})$ and 3d electrons and that between a hole and 4p electrons $n_{l\alpha}^p (= \sum_\sigma P_{l\alpha\sigma}^\dagger P_{l\alpha\sigma})$. t_α^β in $\mathcal{H}_{\text{band}}$ (Eq. (28)) is the hopping integral between NN $4p_\alpha$ orbitals in the β direction, and are parameterized as $t_\alpha^\beta = \delta_{\alpha\beta} t_\sigma^{4p} + (1 - \delta_{\alpha\beta}) t_\pi^{4p}$.

The above model Hamiltonian includes a MnO_6 cluster where electrons couple with the Mn 4p band. Therefore, neither the conventional numerical methods in a small cluster nor the perturbational approaches in terms of the Coulomb interactions are utilized to calculate ASF. The memory-function method (the composite-operator method, the projection method) in the Green's function formalism [136, 164, 165, 166]. is one of the unperturbational methods widely applied to study the electronic structure in solids. It is known that this method is reliable to describe the itinerant and localized nature of correlated electrons on an equal footing. The relevant part of ASF at site l (Eq. (15)) is represented by the Green's function as

$$\text{Im}\Delta f_{l\alpha\alpha} = -\frac{|A_{1s4p}|^2}{m} \sum_\sigma \text{Im}G_{l\alpha\sigma}(\omega + i\Gamma), \quad (30)$$

where $G_{l\alpha\sigma}(\omega)$ is the Fourier transforms of

$$G_{l\alpha\sigma}(t) = \theta(t) \langle i | [J_{l\alpha\sigma}^\dagger(t), J_{l\alpha\sigma}(0)] | i \rangle, \quad (31)$$

with the operator $J_{l\alpha\sigma} = P_{l\alpha\sigma}^\dagger s_{l\sigma}$. It is convenient to introduce the relaxation function (Kubo function) at finite temperature T :

$$\begin{aligned} C_{l\alpha\sigma}(t) &= \theta(t) T \int_0^\beta d\lambda \langle J_{l\alpha\sigma}^\dagger(t) J_{l\alpha\sigma}(i\lambda) \rangle \\ &\equiv \theta(t) \langle J_{l\alpha\sigma}^\dagger(t) J_{l\alpha\sigma}(0) \rangle_\lambda. \end{aligned} \quad (32)$$

There exists the relation between $G_{l\alpha\sigma}$ and $C_{l\alpha\sigma}$:

$$\text{Im}G_{l\alpha\sigma}(\omega) = \beta\omega \text{Im}C_{l\alpha\sigma}(\omega) \Big|_{T \rightarrow 0}. \quad (33)$$

The relaxation function is calculated by utilizing the equations of motion method. The final form is given by the continued fraction form [166]:

$$C_{l\alpha\sigma}(\omega) \equiv \delta M^{(0)}(\omega), \quad (34)$$

with

$$\delta M^{(n-1)}(\omega) = \frac{I^{(n)}}{\omega - (M_0^{(n)} + \delta M^{(n)}(\omega))I^{(n-1)}}, \quad (35)$$

for $n \geq 1$. $I^{(n)}$ is the normalization factor

$$I^{(n)} = \langle \psi_n^\dagger \psi_n \rangle_\lambda, \quad (36)$$

and $M_0^{(n)}$ is the static part of the self-energy

$$M_0^{(n)} = \langle (i\partial_t \psi_n^\dagger) \psi_n \rangle_\lambda, \quad (37)$$

where ψ_n is the operator product (the composite operator) defined by

$$(\psi_1, \psi_2, \psi_3) = (J_{l\alpha\sigma}, P_{l\alpha\sigma}^\dagger s_{l\sigma} \delta n_{l\gamma}^d, P_{l\alpha\sigma}^\dagger s_{l\sigma} \delta n_{l\gamma}^{dp}), \quad (38)$$

with $\delta A = A - \langle A \rangle$ and $n_{l\gamma}^{dp} = \sum_\sigma d_{l\gamma\sigma}^\dagger p_{l\gamma\sigma}$. These operators are treated as single quantum variables describing well-defined excitations in a system [166].

Advantages of the memory functional method in this issue are the following: (1) The many-body excitations arising from the local Coulomb interactions in a MnO_6 cluster are treated by the composite operator ψ_n in Eq. (38). For example, the operator product $\psi_2 = P_{i\alpha\sigma}^\dagger s_{i\sigma} n_{i\gamma}^{dp}$ describes the dipole transition from the Mn $1s$ to $4p$ orbitals associated with the charge transfer from O $2p$ to Mn $3d$ orbitals. This corresponds to the so-called well-screened intermediate state described by $|\underline{1s} \ 3de_g^2 \ 4p^1 \ \underline{L}\rangle$ where \underline{L} indicates that a hole occupies the ligand O $2p$ orbitals. The energy of this many-body excitation is lower than that of the so-called poor screened state $|\underline{1s} \ 3de_g^1 \ 4p^1\rangle$ where the excitation is described by the operator $\psi_0 = P_{i\alpha\sigma}^\dagger s_{i\sigma}$. It is experimentally confirmed in several transition-metal oxides that the well-screened state dominates the final state of XAS and the intermediate state of RXS [167, 168, 169, 170, 171, 172, 173, 174]. By treating the operator products as single quantum variables, the many-body excitations and the configuration interactions between them are taken into account in this formalism. These are important on the calculation of ASF and are not taken into account by the independent single-particle scheme with an averaged potential, such as the LDA band calculation [140, 142]. (2) The itinerant effects of the $4p$ electrons are included in $\delta M^{(n)}$. By applying the loop approximation in the diagrammatic technique to some terms in $\delta M^{(n)}$, the itinerant character of the excited electron is taken into account. This effect is of crucial importance to describe the energy dependent ASF, since the band width of the Mn $4p$ electron is of the order of 10eV . This is not well described by the calculations in a small size cluster [134, 141].

The calculated ASF in RXS is presented in Fig. 15 [136, 138]. The $[3d_{3x^2-r^2}/3d_{3y^2-r^2}]$ -type orbital ordered state, where the $3d_{3x^2-r^2}$ and $3d_{3y^2-r^2}$ orbitals are alternately ordered in the ab plane in a cubic crystal, are considered and ASF at the $3d_{3x^2-r^2}$ orbital occupied site is shown. The parameter values in the Hamiltonian are chosen to be $\varepsilon_p - \varepsilon_d = 1.5$, $t_\sigma^{4p} = 3.5$, $t_\pi^{4p} = t_\sigma^{4p}/4$, $U = 5$, $U' = 4$, $J_H = I = 1$, $V_{sd} = -5$, $V_{sp} = -3.5$, $F_0(3d, 4p) = 3.5$, $F_2(3d, 4p) = 0.25$ and $\Gamma = 1.5$ in units of t_{pd} being about $1\sim 1.5$ eV. Some of these values are determined by considering the analyses

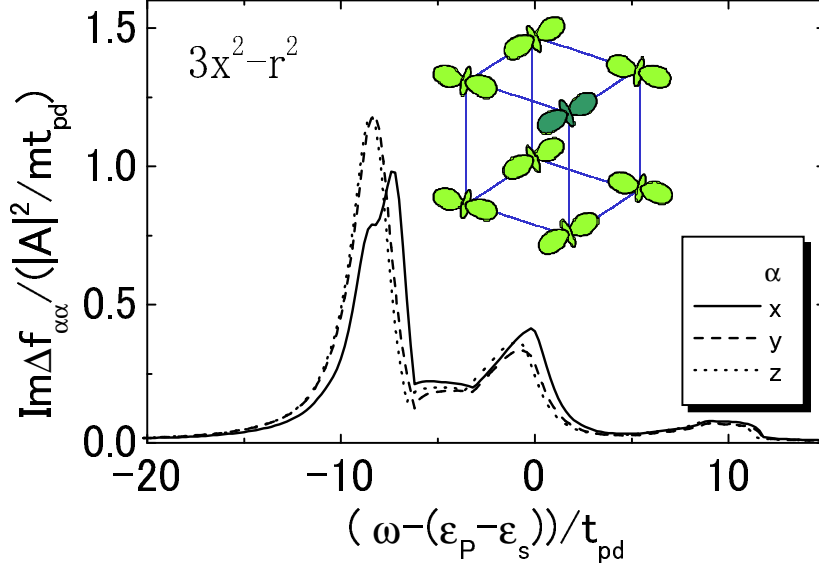


Figure 15. The energy dependence of the imaginary part of ASF. The $3d_{3x^2-r^2}$ orbital is occupied in the $[3d_{3x^2-r^2}/3d_{3y^2-r^2}]$ -type orbital ordered state. The full, dashed and dotted lines indicate ASF for $\alpha = x, y$ and z , respectively. The inset shows a schematic picture of this orbital ordered state [138].

of the photoemission and x-ray absorption experiments (Refs. [175, 176, 177, 168]). It is interpreted that the present value of $F_2(3d, 4p)$ includes the effects of the inter-site Coulomb interaction (Eq. (20)) which is not considered explicitly in the model Hamiltonian (Eq. (23)). This is because (1) these two interactions contribute to the anisotropy of ASF cooperatively, and (2) the inter-site Coulomb interaction has a large contributions in the well screened state dominating the intermediate state of RXS. In Fig. 15, the lower edge of the spectra around $(\omega - (\varepsilon_P - \varepsilon_s))/t_{pd} = -10$ corresponds to the K absorption edge of the Mn ion. $\text{Im}\Delta f_{l\alpha\alpha}$ shows a continuous spectra which spread over a wide region of energy ω . The spectra reflect a broad width of the Mn $4p$ band. However, the energy dependence of $\text{Im}\Delta f_{l\alpha\alpha}$ is not the $4p$ density of states itself; there exist several peak structures in $\text{Im}\Delta f_{l\alpha\alpha}$ which originate from the local excitations in the MnO_6 cluster. Near the absorption edge, the anisotropy between $\text{Im}\Delta f_{lxx}$ and $\text{Im}\Delta f_{lyy(zz)}$ is shown and $\text{Im}\Delta f_{lyy(zz)}$ governs the intensity. This anisotropy is caused by the Coulomb interaction between $3d$ and $4p$ electrons which pushes up the $4p_x$ band at the $3d_{3x^2-r^2}$ orbital occupied site. The core hole potential makes the anisotropy remarkable, since the potential reduces the energy of the dipole transition and enhances the local character of the $4p$ electrons. The scattering intensity of RXS, $I = (mt_{pd}/2|A_{1s4p}|)^2 |(\Delta f_{lxx} - \Delta f_{lyy})|^2$, is shown in Fig. 16 associated with the experimental data in $\text{Nd}_{0.55}\text{Sr}_{0.45}\text{MnO}_3$ [115]. A sharp peak structure near the K edge together with a small intensity above the edge appears in ASF. Both structures

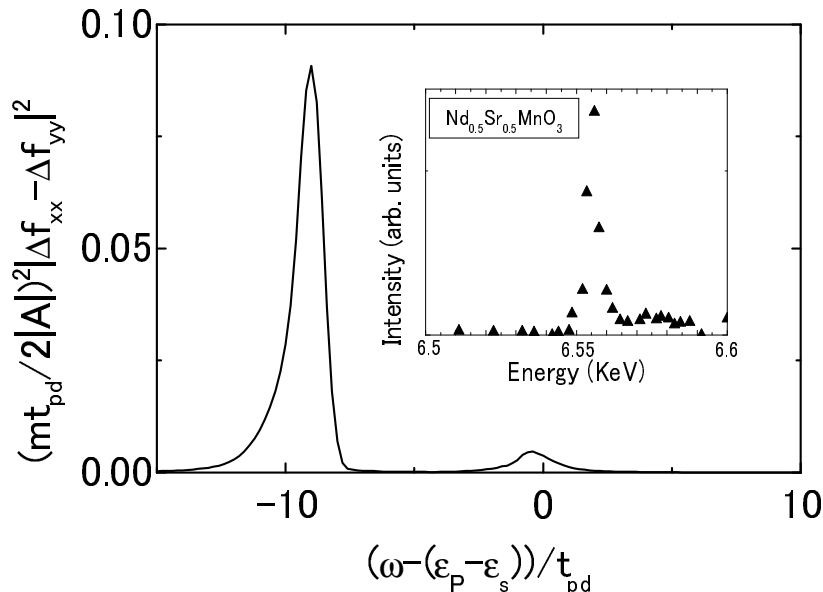


Figure 16. The energy dependence of the scattering intensity of RXS in the $[3d_{3x^2-r^2}/3d_{3y^2-r^2}]$ -type orbital ordered state [138]. The inset is the experimental results of the scattering intensity in $\text{Nd}_{0.5}\text{Sr}_{0.5}\text{MnO}_3$ [115].

were confirmed in the experimental spectra in several manganites with orbital order [112, 117, 120].

In the last part of this subsection, we review other theoretical examinations of RXS in orbital ordered state. In several cases of the orbital ordering, the direct access of RXS to the orbital concerned were examined. The orbital ordering in $\text{La}_{1.5}\text{Sr}_{1.5}\text{MnO}_4$ has a unit cell with $\sqrt{2}a \times 2\sqrt{2}a \times c$ (Fig. 3). As pointed out in Ref. [147], it is barely possible to satisfy the diffraction condition for RXS at the Mn L edge; $2\sqrt{2}a \sim 11\text{\AA}$ and the wave length of x ray is about 20\AA . Here, an electron is directly excited to the Mn $3d$ orbitals from the Mn $2p$ ones. Another possibility was proposed in the orbital ordered system where the local inversion symmetry is broken at the transition metal site. The unoccupied $3d$ states mix with the $4p$ states which are directly accessed by RXS at the K edge. The experimental results of RXS in V_2O_3 [114] were compared with the theoretical calculations of the possible orbital ordered states (Refs. [113, 178, 179, 180]). RXS at the M edge of a $5f$ ion is also possible to directly access to the $5f$ orbital by the transition of $3d \rightarrow 5f$. RXS experiments was performed in UPd_3 [131] where x ray with the wave length of 3.5\AA was utilized. This process was proposed theoretically in URu_2Si_2 [148]. RXS in the orbital ordered state was also examined from the phenomenological point of view in Ref. [146]. The x-ray susceptibility tensor was formulated in the system where the several anisotropic factors due to the spin, orbital and lattice degrees of freedom coexist. The forbidden reflections caused by the combined effects among them were pointed out. This approach may have relation to the theoretical framework of RXS

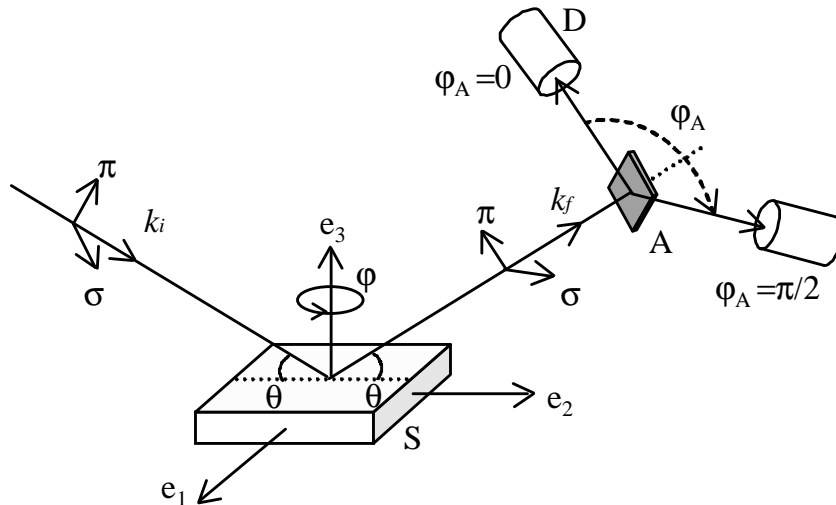


Figure 17. An experimental arrangement of RXS consisting of a sample crystal (S), an analyzer crystal (A) and a photon detector (D). \vec{k}_i and \vec{k}_f are the incident and scattered x-ray momenta, φ is the azimuthal angle, φ_A is the analyzer angle and θ_s is the scattering angle [107, 135].

presented in Sec. 3.4.

3.3. Azimuthal angle dependence

Once the matrix elements of ASF tensor are obtained microscopically, the scattering intensity in RXS is calculated in a realistic experimental arrangement. One of the important experimental parameters is the azimuthal angle (φ) which is a rotation angle in terms of the scattering vector. As mentioned previously, the tensor character of ASF due to the orbital order is directly observed through the φ dependent scattering intensity. In this subsection, the general formulas of the scattering intensity by taking into account the experimental arrangements are derived and a validity of the φ dependent scattering intensity to study the orbital ordering is demonstrated. Experimental results observed in layered manganites $\text{La}_{2-2x}\text{Sr}_{1+2x}\text{Mn}_2\text{O}_7$ are also reviewed.

Consider an experimental arrangement of RXS applied to orbital ordered compounds (Fig. 17 [107]). It consists of a sample crystal (S), a polarization analyzer including an analyzer crystal (A), and a photon detector (D). The polarization scan is characterized by two rotation angles, i.e. the azimuthal angle (φ) and the analyzer angle (φ_A). The former is the rotation angle of the sample around the scattering vector $\vec{K} = \vec{k}_i - \vec{k}_f$, and the latter is that of the analyzer around an axis which is parallel to the scattered photon momentum. We assume that the incident x ray is perfectly polarized in the horizontal plane, i.e. σ -polarization. A direction of the electric vector

of the incident x ray with respect to the crystalline axis is changed by the azimuthal rotation. Because of the tensor character of ASF, the scattered x ray has both the π - and σ -polarized components, which are separated by the analyzer scan. In this optical arrangement, the scattering intensity is given by [135]

$$I(\varphi, \varphi_A) = \sum_{\lambda} \left| \sum_{\lambda_f} M_{\lambda\lambda_f}(\varphi_A) A_{\lambda_f\lambda_i}(\varphi) \right|^2, \quad (39)$$

where λ and $\lambda_{i(f)}$ ($= \pi, \sigma$) indicate the polarization of x ray. $M_{\lambda'\lambda}(\varphi_A)$ is the scattering matrix of the analyzer:

$$M(\varphi_A) = F_A \begin{pmatrix} \cos \varphi_A & -\sin \varphi_A \\ \sin \varphi_A \cos 2\theta_A & \cos \varphi_A \cos 2\theta_A \end{pmatrix}, \quad (40)$$

with the scattering factor $|F_A|$ and the scattering angle θ_A in the analyzer crystal. For simplicity, θ_A is fixed to be $\pi/4$ from now on. The σ - and π -polarized components in the scattered x ray are separately detected by a detector with $\varphi_A = 0$ and $\pi/2$, respectively. The scattering amplitude $A_{\lambda_f\lambda_i}(\varphi)$ is defined by

$$A_{\lambda_f\lambda_i}(\varphi) = \frac{e^2}{mc^2} \vec{e}_{k_f\lambda_f} \left[U(\varphi) V F V^\dagger U(\varphi)^\dagger \right] \vec{e}_{k_i\lambda_i}^t, \quad (41)$$

where $F_{\alpha\beta}$ is the structure factor given in the coordinate of the crystallographic axis $(\hat{a}, \hat{b}, \hat{c})$. The polarization vectors of incident and scattered x ray are given by

$$\begin{aligned} \vec{e}_{k_i\sigma} &= (1, 0, 0), \\ \vec{e}_{k_f\sigma} &= (1, 0, 0), \\ \vec{e}_{k_i\pi} &= (\sin \theta, \cos \theta, 0), \\ \vec{e}_{k_f\pi} &= (-\sin \theta, \cos \theta, 0). \end{aligned} \quad (42)$$

The unitary matrix $U(\varphi)$ in Eq. (41) describes the azimuthal rotation of the sample around the \hat{e}_3 axis and the matrix V governs the transformation from a coordinate of the crystallographic axis $(\hat{a}, \hat{b}, \hat{c})$ to the laboratory system $(\hat{e}_1, \hat{e}_2, \hat{e}_3)$. $F_{\alpha\beta}$ is the structure factor given by

$$F_{\alpha\beta} = N \sum_{l \in \text{cell}} e^{i(\vec{k}_i - \vec{k}_f) \cdot \vec{r}_l} f_{l\alpha\beta}, \quad (43)$$

with the number of unit cell N . When the matrix V and the tensor elements of ASF $f_{l\alpha\beta}$ are identified, the scattering intensity is calculated as a function of the azimuthal angle φ .

We introduce the following three cases where the above formulas are applied to the orbital ordered states [135]. (1) *the orbital superlattice reflection*: Consider the orbital ordered state where two different kinds of orbitals are ordered in a simple cubic lattice. This state is termed antiferro(AF)-type orbital ordered state, on the analogy of the antiferromagnetic state. In particular, the C -type AF orbital ordered state, where two different orbitals are alternately aligned in the ab plane, is widely observed in manganites. RXS at $(h k l) = (\frac{2l+1}{2} \frac{2m+1}{2} n)$ termed the orbital superlattice reflection, appears in this state. Consider the case $l = m$. The explicit form of the scattering

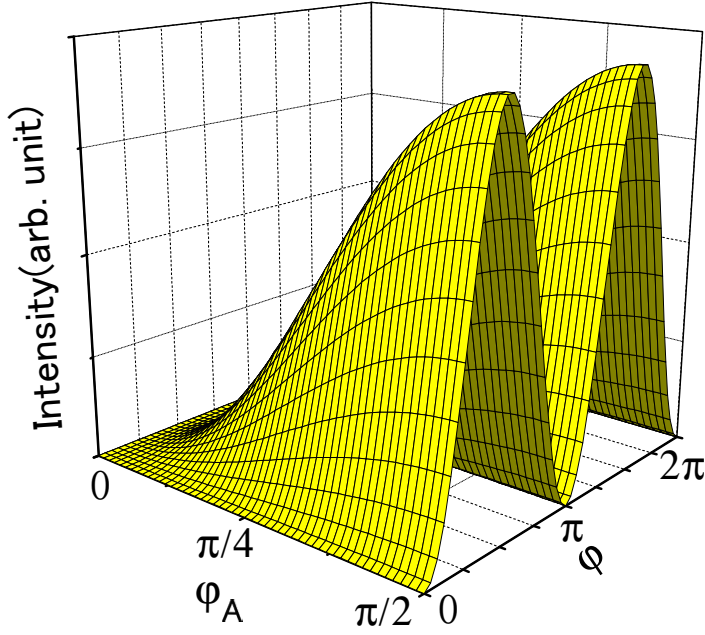


Figure 18. The azimuthal and analyzer angle dependences of the RXS intensity at the orbital superlattice reflection [135].

intensity $\tilde{I}(\varphi, \varphi_A)$ at this reflection point normalized by a factor $N^2 \sigma_T |F_A|^2$ is obtained as:

$$\tilde{I}(\varphi, \varphi_A = 0) = |\Delta f_{-zz} \cos^2 \varphi + \frac{1}{2}(\Delta f_{-xx} + \Delta f_{-yy}) \sin^2 \varphi|^2, \quad (44)$$

and

$$\begin{aligned} \tilde{I}(\varphi, \varphi_A = \frac{\pi}{2}) &= |\frac{1}{2}(-\Delta f_{-xx} + \Delta f_{-yy}) \sin \varphi \cos \theta \\ &+ \frac{1}{2}(\Delta f_{-xx} + \Delta f_{-yy} - 2\Delta f_{-zz}) \sin \varphi \cos \varphi \sin \theta|^2, \end{aligned} \quad (45)$$

which correspond to the scattering intensity with $\lambda_i = \lambda_f = \sigma$ ($\sigma - \sigma$ scattering), and that with $\lambda_i = \sigma$ and $\lambda_f = \pi$ ($\sigma - \pi$ scattering), respectively. $\Delta f_{-\alpha\alpha}$ is termed the AF component of ASF defined by $\Delta f_{-\alpha\alpha} = \frac{1}{2}(\Delta f_{A\alpha\alpha} - \Delta f_{B\alpha\alpha})$ where $\Delta f_{A(B)}$ is the anomalous part of ASF for the $A(B)$ orbital sublattice. In particular, consider the $[\theta_A/\theta_B = -\theta_A]$ -type orbital ordered state where the following conditions are satisfied; $\Delta f_{Axx} = \Delta f_{Byy}$, $\Delta f_{Ayy} = \Delta f_{Bxx}$ and $\Delta f_{Azz} = \Delta f_{Bzz}$. The intensity is simplified as

$$\tilde{I}(\varphi, \varphi_A = 0) = 0, \quad (46)$$

and

$$\tilde{I}(\varphi, \varphi_A = \frac{\pi}{2}) = |\Delta f_{-xx}|^2 \sin^2 \varphi \cos^2 \theta. \quad (47)$$

A whole feature of $\tilde{I}(\varphi, \varphi_A)$ is shown in Fig. 18. $\tilde{I}(\varphi, \varphi_A = \pi/2)$ shows a square of the sinusoidal curve. The intensity becomes its maximum (minimum) at $\varphi = (2n + 1)\pi/2$

($\varphi = n\pi$) where the electric field of incident x ray is parallel to the ab plane (the c axis). This is explained by the fact that the AF component of ASF $\Delta f_{-\alpha\alpha}$ is zero for $\alpha = z$ and is finite for $\alpha = x$ and y . Note that the φ dependence of the scattering intensity in other types of orbital ordered state is distinct from the above results. It has been experimentally confirmed, in several perovskite manganites, that the observed φ dependence at the orbital superlattice reflection is well fitted by Eqs. (46) and (47). Then, it is concluded that the orbital ordered state in these compounds to be of the $[\theta_A / -\theta_A]$ -type, although a value of θ_A is not determined.

As shown above, the AF component of ASF, $\Delta f_{-\alpha\alpha}$, is observed at the orbital superlattice reflection, because a phase of x ray at the orbital sublattice A is different from that at B by π . On the other hand, the ferro(F)-component of ASF defined by $\Delta f_{+\alpha\alpha} = \frac{1}{2}(\Delta f_{A\alpha\alpha} + \Delta f_{B\alpha\alpha})$ is not detected at this reflection. The F component of ASF reflects from the uniform shape of orbital. A value of θ_A in the $[\theta_A / \theta_B = -\theta_A]$ -type orbital ordered state can be determined by $\Delta f_{+\alpha\alpha}$. We introduce, in the following, the two possible methods by which the F component of ASF is observed. (2)*the fundamental reflection*: The F component of ASF directly reflects the scattering intensity at the fundamental reflection point denoted by $(h k l) = (l m n)$. The scattering intensity at this point is given by

$$\tilde{I}(\varphi, \varphi_A = 0) = |\Delta f_{+xx} \cos^2 \varphi + \Delta f_{+zz} \sin^2 \varphi + f_{0+}|^2, \quad (48)$$

where f_{0+} is defined by $f_{0+} = \frac{1}{2}(f_{0A} + f_{0B})$. f_{0+} is a scalar and does not show the φ dependence. Thus, the F component of ASF, $\Delta f_{+\alpha\alpha}$, is observed by the azimuthal scan. This is an analogous to the fact that the ferromagnetic component is obtained through the polarization analyses of the neutron scattering. Since, even in the resonant scattering, the scattering intensity from f_0 is usually larger than that from $\Delta f_{+\alpha\alpha}$, the interference effects between the normal and anomalous parts of ASF in Eq. (48) dominates the φ dependence. In an actual experiment, a higher order reflection is effective, since f_0 decreases rapidly with $|K|$ in contrast to $\Delta f_{+\alpha\alpha}$. A small tip of the azimuth rotation axis from the crystallographic axis is useful to measure this interference effect, as recently performed in some manganites [124]. (3)*the charge order superlattice reflection*: When the orbital order appears associated with the charge order, the F component of ASF is obtained by utilizing the φ dependent RXS intensity at the charge superlattice reflection. Consider the charge and orbital ordered state observed in manganites around hole concentration being 0.5 (see Fig. 3). The charge order is observed by RXS at $(h k l) = (\frac{2l+1}{2} \frac{2m+1}{2} n)$ termed the charge superlattice reflection. In the case of $l = m$, the scattering intensity is given by

$$\tilde{I}(\varphi, \varphi_A = 0) = \frac{1}{4} |\Delta f_{+xx} \sin^2 \varphi + \Delta f_{+zz} \cos^2 \varphi - \Delta f_4|^2, \quad (49)$$

where Δf_4 is the anomalous part of ASF for Mn^{4+} which is independent of the polarization of x ray. Thus, the interference term of Δf_4 and $\Delta f_{+\alpha\alpha}$, as well as a term $|\Delta f_{+\alpha\alpha}|^2$, gives rise to the φ dependent intensity. A much remarkable φ dependence is expected in comparison with that in the case (2) [135, 115].

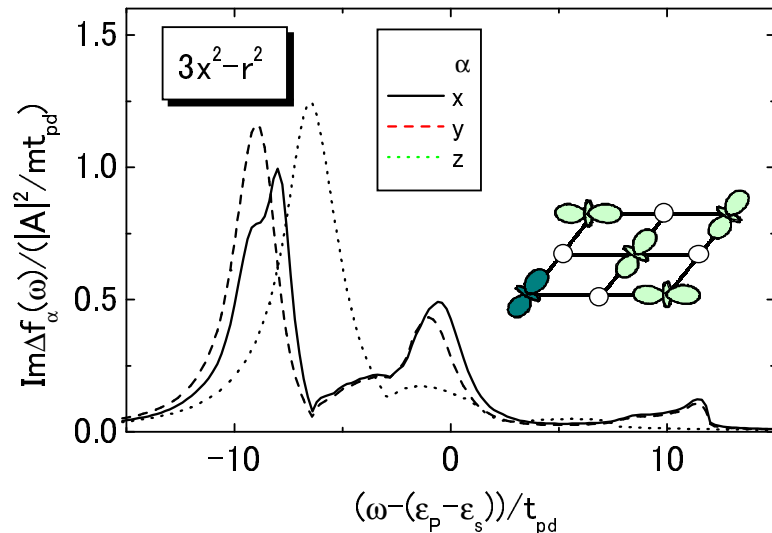


Figure 19. The energy dependence of the imaginary part of ASF in the layered manganites. The $3d_{3x^2-r^2}$ orbital is occupied in the $[3d_{3x^2-r^2}/3d_{3y^2-r^2}]$ -type orbital ordered state. The full, dashed and dotted lines indicate ASF for $\alpha = x, y$ and z , respectively. Inset shows a schematic picture of the charge and orbital ordered state [136].

So far, assuming that a crystal lattice has the cubic symmetry, the azimuthal angle dependence of RXS have been studied. Now we introduce another example of the φ dependent scattering intensity from the charge and orbital orderings in a layered manganites $\text{La}_{2-2x}\text{Sr}_{1+2x}\text{Mn}_2\text{O}_7$ [120, 136]. This compound is recognized to be a material appropriate for studying orbital degree of freedom [181, 182, 183, 184, 185, 186, 187, 188, 189], because the spin and orbital states are systematically changed with the hole concentration. In $\text{LaSr}_2\text{Mn}_2\text{O}_7$ ($x = 0.5$), the charge and orbital ordering appears between about 100K and 210K [120]. Since a MnO_6 octahedron in this compound is almost isotropic, the energy levels of the two e_g orbitals as well as the three $4p$ orbitals are nearly degenerate in the local sense. On the other hand, the layered structure provides the quasi-two dimensional character of the $4p$ band and lifts the degeneracy. Therefore, both the layered structure as well as the orbital ordering are crucially important on the anisotropy in ASF. ASF in this compound was formulated by utilizing the memory function method introduced in Sec. 3.2. The calculated ASF at the $d_{3x^2-r^2}$ orbital occupied site in the $[d_{3x^2-r^2}/d_{3y^2-r^2}]$ -type orbital ordered state is presented in Fig. 19. The parameter values are the same as those in Fig. 15, except for the hopping integral t_α^β between the Mn $4p$ orbitals in Eq. (28); by considering the symmetry, t_α^β is parameterized as $t_x^x = t_y^y \equiv t_\sigma^\parallel$, $t_z^z = t_y^y = t_x^x = t_y^y \equiv t_\pi^\parallel$, $t_z^z \equiv t_\sigma^\perp$ and $t_x^z = t_y^z \equiv t_\pi^\perp$. The anisotropy of the hopping integral due to the layered crystal

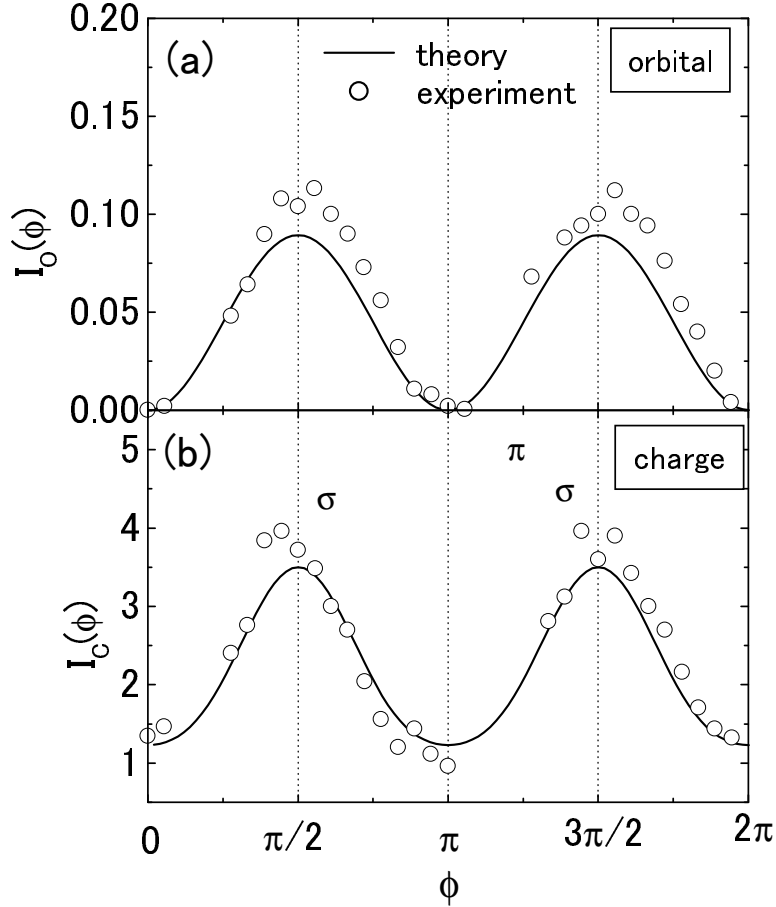


Figure 20. The azimuthal angle dependence of the scattering intensities at the orbital superlattice reflection (a) and at the charge superlattice one (b) near the edge ($(\omega - (\varepsilon_P - \varepsilon_s))/t_{pd} = -9.6$). The solid curves show the intensities in the $[d_{3x^2-r^2}/d_{3y^2-r^2}]$ -type orbital ordered states. The open circles show the experimental data in $\text{LaSr}_2\text{Mn}_2\text{O}_7$ [120]. Absolute values of the experimental data are arbitrary. [136].

is introduced by $t_{\sigma}^{\parallel}/t_{\sigma}^{\perp} = t_{\pi}^{\parallel}/t_{\pi}^{\perp} = 4$. $(\omega - (\varepsilon_P - \varepsilon_s))/t_{pd} = -10$ corresponds to the K -edge. The weight near the K edge is dominated by $\text{Im}\Delta f_{lxx}$ and $\text{Im}\Delta f_{lyy}$, in contrast to the results for the cubic manganites (Fig. 15) where weights of $\text{Im}\Delta f_{lyy}$ and $\text{Im}\Delta f_{lzz}$ are larger than that of $\text{Im}\Delta f_{lzz}$. This is because the $4p_{x(y)}$ band is broader than the $4p_z$ band in the layered crystal structure. The φ dependences of the scattering intensities at the orbital and charge superlattice reflections were calculated by Eqs. (47) and (49), respectively. The results together with the experimental data in $\text{LaSr}_2\text{Mn}_2\text{O}_7$ are presented in Fig. 20. The polarization dependences of the scattering intensity at the orbital and charge superlattice reflection are ascribed to the anisotropies between Δf_{xx} and Δf_{yy} due to the local Coulomb interactions and between $\Delta f_{xx} + \Delta f_{yy}$ and Δf_{zz}

due to the effects of the $4p$ band, respectively. This figure shows good agreement with theory and experiment. In conclusion, from the present comparisons, the $[\theta_A / -\theta_A]$ -type orbital ordered state is realized in $\text{LaSr}_2\text{Mn}_2\text{O}_7$, and the difference between $\Delta f_{lxx(yy)}$ and Δf_{lzz} is dominated by the anisotropy of the $4p$ band.

3.4. General theoretical framework of RXS - orbital ordering, fluctuation and excitations -

In the previous two subsections, we introduced the mechanism of the anisotropy of ASF in orbital ordered state and calculated the energy, polarization and orbital dependence of ASF from the microscopic view points. The model Hamiltonian includes a number of degrees of freedom and several interactions among them. This is a standard procedure for analyses of solid state spectroscopy. However, the main purpose of RXS is to detect the orbital degree of freedom of a $3d$ electron and to reveal their roles in correlated electron systems. For this purpose, we introduce, in this section, a general theoretical framework of RXS which is directly connected with the orbital degree of freedom of a $3d$ electron [137]. The obtained form is applied to study the orbital ordering, fluctuation and excitations.

Let us start with the differential scattering cross section given in Eq. (7). This equation is rewritten by using the correlation function of the electronic polarizability $\alpha_{\beta\alpha}$:

$$\frac{d^2\sigma}{d\Omega d\omega_f} = \sigma_T \frac{\omega_f}{\omega_i} \sum_{\alpha\beta\alpha'\beta'} P_{\beta'\alpha'} P_{\beta\alpha} \Pi_{\beta'\alpha'\beta\alpha}(\omega, \vec{K}), \quad (50)$$

where

$$\Pi_{\beta'\alpha'\beta\alpha}(\omega, \vec{K}) = \frac{1}{2\pi} \int dt e^{i\omega t} \sum_l e^{-i\vec{K}\cdot(\vec{r}_{l'}-\vec{r}_l)} \langle i | \alpha_{l'\beta'\alpha'}(t)^\dagger \alpha_{l\beta\alpha}(0) | i \rangle, \quad (51)$$

with $\vec{K} = \vec{k}_i - \vec{k}_f$, $\omega = \omega_i - \omega_f$ and $P_{\beta\alpha} = (\vec{e}_{k_f\lambda_f})_\beta (\vec{e}_{k_i\lambda_i})_\alpha$. $\alpha_{l\beta\alpha}(t)$ is the polarizability operator $\alpha_{l\beta\alpha}^{(\omega_i)}$ at site l [101, 102, 190, 191, 192];

$$\alpha_{l\beta\alpha}(t) = e^{i\mathcal{H}_e t} \alpha_{l\beta\alpha}^{(\omega_i)} e^{-i\mathcal{H}_e t}, \quad (52)$$

where \mathcal{H}_e is the electronic part of the Hamiltonian (Eq. (5)) and $\alpha_{l\beta\alpha}^{(\omega_i)}$ is given by

$$\alpha_{l\beta\alpha}^{(\omega_i)} = i \int_{-\infty}^0 dt e^{-i\omega_i t} [j_{l\beta}(0), j_{l\alpha}(t)]. \quad (53)$$

This definition of $\alpha_{l\beta\alpha}^{(\omega_i)}$ corresponds to the form of $S_{2\alpha\beta}$ given in Eq. (9), when $\vec{j}(\vec{k})$ is replaced by \vec{j}_l .

Now the polarizability operator $\alpha_{l\beta\alpha}$ defined at site l is expanded in terms of the electronic operators of $3d$ electrons by utilizing the group theoretical analyses. Consider the O_h point symmetry around a Mn ion and the doubly degenerate orbitals with the E_g symmetry in each Mn site. The pseudo-spin operators are introduced as

$$T_{l\mu} = \frac{1}{2} \sum_{\gamma\gamma'\sigma} d_{l\gamma\sigma}^\dagger (\sigma_\mu)_{\gamma\gamma'} d_{l\gamma'\sigma}, \quad (54)$$

for $\mu = (0, x, y, z)$ where σ_0 is a unit matrix and σ_ν ($\nu = x, y, z$) are the Pauli matrices. $T_{l\mu}$'s represent the charge ($\mu = 0$) and orbital ($\mu = x, y, z$) degrees of freedom of a $3d$ electron at site l and have the A_{1g} , E_{gv} , A_{2g} and E_{gu} symmetries for $\mu = 0, x, y$ and z , respectively. When $\alpha_{l\beta\alpha}$ associated with a pseudo-spin operator at site l is considered, $\alpha_{l\beta\alpha}$ is expressed by products of $T_{l\mu}$ and a tensor with respect to the polarizations of x ray. This tensor has $T_{1u} \times T_{1u}$ symmetry being reduced to $A_{1g} + E_g + T_{1g} + T_{2g}$. Since the polarizability should have the A_{1g} symmetry, $\alpha_{l\beta\alpha}$ is expressed as

$$\alpha_{l\beta\alpha} = \delta_{\alpha\beta} I_{A_{1g}} T_{l0} + \delta_{\alpha\beta} I_{E_g} \left(\cos \frac{2\pi n_\alpha}{3} T_{lz} - \sin \frac{2\pi n_\alpha}{3} T_{lx} \right). \quad (55)$$

$(n_x, n_y, n_z) = (1, 2, 3)$ and $I_{A_{1g}(E_g)}$ is a constant which is not determined by the group theoretical analyses. Note the following characteristics in Eq. (55): (A) Higher order terms with respect to $T_{l\mu}$ at site l , e.g. $T_{lx}T_{lz}$, are reduced to the linear terms of $T_{l\mu}$ by using the SU(2) algebra of $\vec{T}_{l\mu}$. (B) The terms including $T_{m \neq l\mu}$, such as $T_{lx}T_{mz}$, are neglected. These terms are caused by the higher order processes of the electron hopping and the inter-site Coulomb interactions. (C) T_{ly} describing the magnetic octupole moment [86, 87, 88] does not appear in Eq. (55). This is because the coupling constant of $\alpha_{l\beta\alpha}$ does not include the A_{2g} symmetry. (D) Spin operators are not included. This is because the spin-orbit coupling is quenched in the e_g orbital states in a Mn ion. The magnetic diffraction intensity is expected to be small in RXS at K -edge in antiferromagnets with linearly polarized x ray. (E) Microscopic origins of the $\vec{T}_{l\mu}$ dependent polarizability are introduced in Sec. 3.2, i.e. the Coulomb and Jahn-Teller mechanisms, where the $1s \rightarrow 4p$ transition reflects the $3d$ orbital states through the Coulomb interactions and the lattice distortions, respectively. However, it is noted that Eq. (55) is derived by only considering the symmetry of crystal structure and orbitals.

By using Eq. (55), Eq. (51) is rewritten as

$$\begin{aligned} \Pi_{\beta'\alpha'\beta\alpha}(\omega, \vec{K}) &= \delta_{\beta'\alpha'} \delta_{\beta\alpha} \frac{1}{2\pi} \int dt e^{i\omega t} \sum_{l'l} e^{-i\vec{K} \cdot (\vec{r}_{l'} - \vec{r}_l)} \\ &\times \sum_{\gamma, \gamma'=0, x, z} I_{\gamma'\alpha'} I_{\gamma\alpha} \langle T_{l'\gamma'}(t) T_{l\gamma}(0) \rangle, \end{aligned} \quad (56)$$

with $I_{0\alpha} = I_{A_{1g}}$ and $I_{x(z)\alpha} = I_{E_g} \cos(-\sin) \frac{2\pi n_\alpha}{3}$. The scattering cross section of RXS is directly connected to the dynamical correlation function of the pseudo-spin operators. The equation (50) with Eq. (56) is analogous to the scattering cross section in the magnetic neutron and conventional x-ray/electron scatterings which are represented by the correlation functions of spin and charge, respectively. In the following, the cross section given in Eq. (50) with Eqs. (51) and (56) is applied to the scatterings from orbital ordering, fluctuation and excitations.

(1) *Static scattering from orbital ordering*: In the static scattering where the scattered x-ray energy is integrated out, the cross section is given by the equal-time correlation function:

$$\frac{d\sigma}{d\Omega} = \sigma_T \sum_{\alpha\alpha'} P_{\alpha'\alpha'} P_{\alpha\alpha} \sum_{\gamma, \gamma'=0, x, z} I_{\gamma'\alpha'} I_{\gamma\alpha} S_{\gamma'\gamma}(\vec{K}), \quad (57)$$

with

$$S_{\gamma'\gamma}(\vec{K}) = \sum_{l'} e^{-i\vec{K}\cdot(\vec{r}_{l'}-\vec{r}_l)} \langle T_{l'\gamma'} T_{l\gamma} \rangle. \quad (58)$$

This form is applicable to the scattering from the orbital ordering below the ordering temperature T_{OO} . Consider the C -type AF orbital order of the $[\theta_A/\theta_B]$ -type which is observed in $\text{Pr}_{0.5}\text{Sr}_{0.5}\text{MnO}_3$. The rotating frame is introduced in the pseudo-spin space at each Mn site:

$$\tilde{T}_{lz} = \cos \theta_l T_{lz} - \sin \theta_l T_{lx}, \quad (59)$$

for $l = A$ and B . The scattering cross sections at the orbital superlattice reflection is obtained from Eqs. (57) and (58) as

$$\left. \frac{d\sigma}{d\Omega} \right|_{\sigma \rightarrow \pi} = \sigma_T N^2 3 I_{E_g}^2 \langle \tilde{T}_z \rangle^2 \sin^2 \theta_A \sin^2 \varphi \cos^2 \theta, \quad (60)$$

with $\langle \tilde{T}_z \rangle = \frac{1}{2} \sum_{l=A,B} (\langle \tilde{T}_{Az} \rangle + \langle \tilde{T}_{Bz} \rangle)$, the azimuthal angle φ and the scattering angle θ . The polarizations of the incident and scattered x ray are chosen to be σ and π , respectively, and a relation $\theta_A = -\theta_B$ is assumed. This expression corresponds to Eq. (47). It is worth noting that the cross section is proportional to $(\langle \tilde{T}_z \rangle \sin \theta_A)^2 = \langle (T_{xA} - T_{xB}) \rangle^2$, i.e. a square of the AF component of T_x . Being based on this fact, the following two information for the orbital ordering are obtained from the experimental data. (A) Temperature dependence of the orbital order parameter and its critical exponent β are derived. Near T_{OO} , the RXS intensity is proportional to $(1 - T/T_{OO})^{2\beta}$. (B) The scattering intensity depends on types of the orbital ordered state, i.e. a value of θ_A . The factor $\sin^2 \theta_A$ becomes maximum in the state of $[\frac{1}{\sqrt{2}}(d_{3z^2-r^2} - d_{x^2-y^2})/\frac{1}{\sqrt{2}}(d_{3z^2-r^2} + d_{x^2-y^2})]$ -type ($\theta_A = \pi/2$) rather than the $[d_{x^2-z^2}/d_{y^2-z^2}]$ - ($\theta_A = \pi/3$) or $[d_{3x^2-r^2}/d_{3y^2-r^2}]$ -types ($\theta_A = 2\pi/3$). A complementary information for the orbital ordered state is obtained at the charge superlattice reflection $(h \ k \ l) = (\frac{2l+1}{2} \ \frac{2l+1}{2} \ n)$. The cross section for the $\sigma - \pi$ scattering is given by

$$\left. \frac{d\sigma}{d\Omega} \right|_{\sigma \rightarrow \pi} = \sigma_T N^2 \frac{1}{12} I_{E_g}^2 \langle \tilde{T}_z \rangle^2 \cos^2 \theta_A \sin^2 2\varphi \sin^2 \theta, \quad (61)$$

which is proportional to $(\langle \tilde{T}_z \rangle \cos \theta_A)^2 = \langle (T_{zA} + T_{zB}) \rangle^2$. By combining RXS study at the orbital and charge superlattice reflections, types of the orbital ordered states is expected to be determined.

(2) *Diffuse scattering from the orbital fluctuations*: The scattering cross section given in Eqs. (57) and (58) is also applicable to study the diffuse scattering near T_{OO} . The static correlation function $S_{\gamma'\gamma}(\vec{K})$ around the orbital superlattice reflection near T_{OO} contributes to the critical diffuse scattering in RXS. It is worth mentioning that the diffuse scattering in RXS is directly connected to the correlation function of the orbital fluctuation and each element of $S_{\gamma'\gamma}(\vec{K})$ is obtained by changing the x-ray polarization. This is in contrast to the previous studies of the x-ray/neutron diffuse scatterings near the cooperative Jahn-Teller transition [193, 194, 195]. We demonstrate

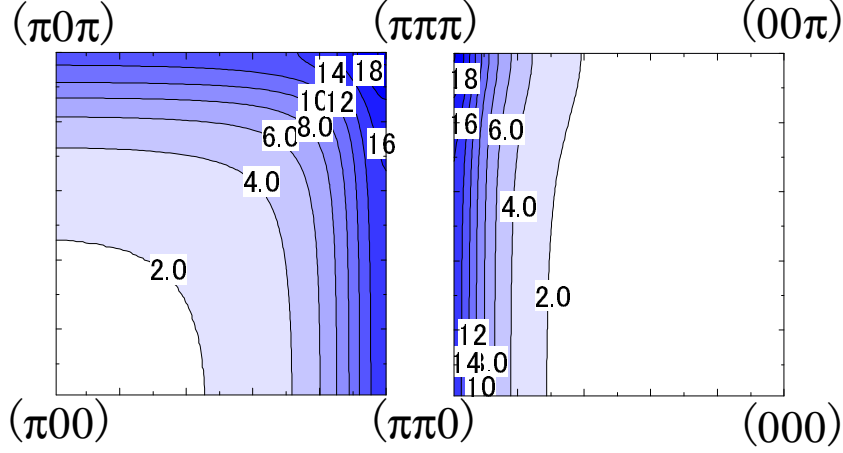


Figure 21. The intensity contour of the diffuse scattering: $B_{xx}(\vec{K}) = (NT\chi_0 I_{E_g}^2)^{-1} \sum_{\gamma'\gamma} I_{\gamma'\alpha} I_{\gamma\alpha} S_{\gamma'\gamma}(\vec{K})$ at $T = 1.05T_{OO}$ [137].

the diffuse scattering in RXS calculated from the model where the interaction between orbitals is caused by the superexchange-type electronic process [34, 49]:

$$\begin{aligned} \mathcal{H}_J = & -2 \sum_{\langle ij \rangle} J_1^l \left(\frac{3}{4} n_i n_j + \vec{S}_i \cdot \vec{S}_j \right) \left(\frac{1}{4} - \tau_i^l \tau_j^l \right) \\ & - 2 \sum_{\langle ij \rangle} J_2^l \left(\frac{1}{4} n_i n_j - \vec{S}_i \cdot \vec{S}_j \right) \left(\frac{3}{4} + \tau_i^l \tau_j^l + \tau_i^l + \tau_j^l \right), \end{aligned} \quad (62)$$

where

$$\tau_i^l = \cos\left(\frac{2\pi n_l}{3}\right) T_{iz} - \sin\left(\frac{2\pi n_l}{3}\right) T_{ix}, \quad (63)$$

with $(n_x, n_y, n_z) = (1, 2, 3)$. l indicates a direction of a bond between site i and its NN site j . J_1^l and J_2^l are the superexchange-type interactions in direction l defined by $J_1^l = t^{l2}/(U' - I)$ and $J_2^l = t^{l2}/U$, and t^l is the hopping integral between the NN Mn sites. This model is known to be suitable to describe the spin and orbital states in an insulating manganite LaMnO_3 [34]. The intensity contour of the diffuse scattering

$$B_{\alpha\alpha}(\vec{K}) = \frac{1}{NT\chi_0 I_{E_g}^2} \sum_{\gamma'\gamma} I_{\gamma'\alpha} I_{\gamma\alpha} S_{\gamma'\gamma}(\vec{K}), \quad (64)$$

was calculated by the random-phase approximation and the numerical results are presented in Fig. 21. The scattering cross section is represented by $B_{\alpha\alpha}$ as follows,

$$\frac{d\sigma}{d\Omega} = ANT\chi_0 I_{E_g}^2 \sum_{\alpha'\alpha} P_{\alpha'\alpha'} P_{\alpha\alpha} B_{\alpha'\alpha}(\vec{K}). \quad (65)$$

The temperature is chosen to be $T = 1.05T_{OO}$. A weak anisotropy in the interactions is introduced as $J_1^{x(y)}/J_1^z = J_1^{x(y)}/J_1^z = \delta_{x(y)}$ with $\delta_x = 1.05$ and $\delta_y = 1.025$ to remove a degeneracy of the orbital ordered state. Below T_{OO} , the orbital order occurs at $(\pi\pi\pi)$. Strong intensity appears along the $(\pi\pi\pi) - (\pi\pi0)$ direction and other two equivalent

ones. This characteristic feature is attributed to the interaction between orbitals adopted above; $J_{xx}(\vec{r}_l - \vec{r}_{l'} = a\hat{z}) = 0$. This arises from the fact that the hopping integral between the $d_{x^2-y^2}$ and $d_{x^2-y^2(3z^2-r^2)}$ orbitals is zero in the z direction.

As introduced in Sec. 2, the temperature dependence of the diffuse scattering was measured in $\text{Pr}_{1-x}\text{Ca}_x\text{MnO}_3$ around $x = 0.4$ [117, 121], although the measurement was carried out along one direction in the Brillouine zone. By applying the Orstein-Zernike theory to $S_{\gamma'\gamma}(\vec{K})$ in Eq. (58), the peak width around the orbital superlattice reflection is given by $\xi(T)^{-1} = \xi_0^{-1} + A(T/T_{OO} - 1)^\nu$ with constants ξ_0 and A , and exponent ν . The experimental data are well fitted by this equation, although more detail measurements are required to determine the precise value of ν , as well as the interaction between orbitals.

(3) *Inelastic scattering from orbital excitations:* In comparison with the orbital ordering, little is known about the orbital excitations and experimental probes to detect them. The optical probes have access directly to the orbital excitations, although the observation is limited to the zero momentum transfer. Recently, a three-peak structure around 150 meV in Raman spectra were observed in LaMnO_3 and were interpreted to be the scattering from the collective orbital excitations termed orbital wave [34, 196, 197, 198]. Now we focus on the inelastic spectroscopy of RXS i.e., the resonant inelastic x-ray scattering (RIXS) as a probe to detect the orbital excitations. This is a momentum resolved probe to detect the bulk electronic structures in solids [199, 200, 201]. Now this experimental technique rapidly progresses accompanied with the recent advances of the third-generation synchrotron light source [174, 202, 203, 204, 205, 206, 207, 208, 209].

Let us consider the orbital excitations in orbital ordered insulating state, such as LaMnO_3 , although the following discussions are applicable to an orbital-ordered metal. The order parameter in the orbital ordered state with the $[3d_{3x^2-r^2}/3d_{3y^2-r^2}]$ -type is represented by the pseudo-spin as

$$\langle \vec{T}_k \rangle = \left(\frac{\sqrt{3}}{4} \delta_{\vec{k}=(\pi\pi 0)}, 0, -\frac{1}{4} \delta_{\vec{k}=(000)} \right), \quad (66)$$

where $\langle \vec{T}_k \rangle$ is the Fourier transform of $\langle \vec{T}_i \rangle$. The orbital excitations are represented by deviations of \vec{T}_i from the above value. There exist two kinds of the orbital excitations: the collective orbital excitation termed the orbital wave and the individual excitation. The orbital wave is analogous to the spin wave in the magnetically ordered states [48, 52, 34, 61, 62, 64, 66]. When an orbital excitation arises at a Mn site, this excitation propagates by interactions between orbitals at different sites denoted by J . Thus, the orbital wave excitations show dispersions and their excitation energies are characterized by J . The energy, dispersion relation and symmetry of the orbital wave were calculated from the model Hamiltonian such as Eq. (62) [34, 197, 210]. The observed peaks by the recent Raman scattering experiment in LaMnO_3 [197] were interpreted to be the scattering from the orbital wave at the point Γ . In contrast to the collective excitations, the individual orbital excitations show continuum spectra. These are analogous to the Stoner excitations in the magnetically ordered states and are arise from the electronic

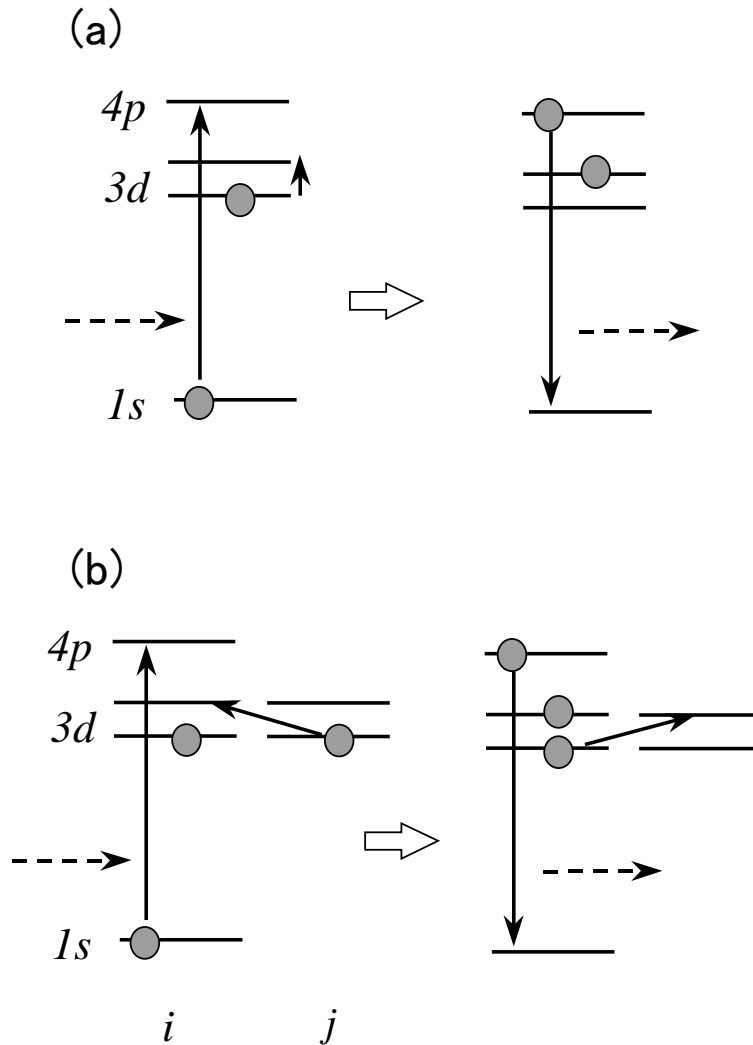


Figure 22. The scattering processes of the orbital excitations in RIXS. The broken arrows indicate incident and scattered x ray [210].

excitations from the lower Hubbard band (the major orbital band) to the upper Hubbard bands (the minor orbital band) across the Mott gap or the charge-transfer gap. Thus, the characteristic energy of the orbital excitations is of the order of the on-site Coulomb interaction U' or the charge transfer energy Δ .

Here we introduce RIXS to detect the orbital excitations. The resonant effect not only enhances the scattering intensity dramatically but also causes several electronic excitations in the intermediate scattering states. It was proposed that the following are the possible scattering processes from the orbital excitations in RIXS [210]: (A) The incident x ray excites an electron from Mn $1s$ orbital to Mn $4p$ one. In the intermediate state, the $3d$ electron is excited from the occupied orbital to the unoccupied one through the Coulomb interaction between $3d$ and $4p$ electrons. Finally, the $4p$ electron fills the

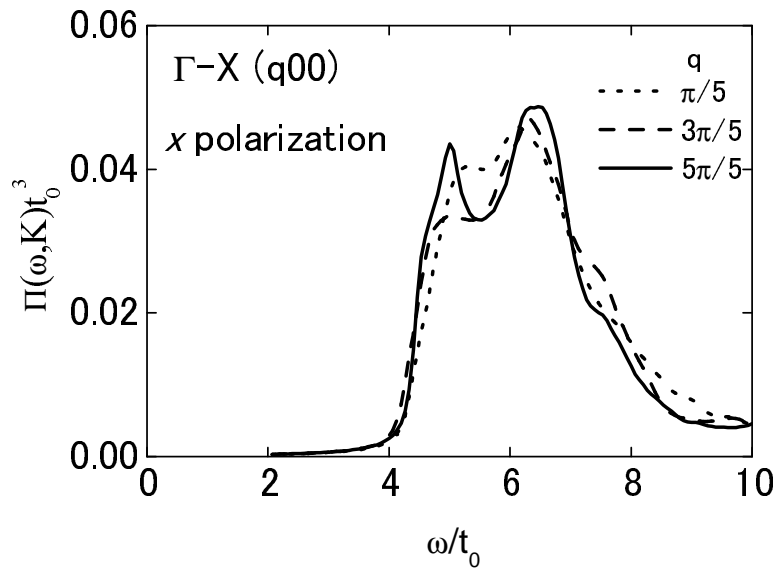


Figure 23. RIXS spectra $\Pi_{\beta'\alpha'\beta\alpha}(\omega, \vec{K})$ for the $[d_{3x^2-r^2}/d_{3y^2-r^2}]$ -type orbital ordered state. The momentum transfer is $\vec{K} = (q00)$ ($\Gamma - X$ direction) in the cubic Brillouin zone. The polarization of x ray is chosen to be $\alpha = \alpha' = \beta = \beta' = x$ (the x polarization). t_0 is estimated to be about $0.5 \sim 0.7$ eV [211].

core hole by emitting x ray. This process is denoted by

$$|3d_{\gamma}^1\rangle + \hbar\omega_i \rightarrow |3d_{\gamma}^1 4p^1 \underline{1s}\rangle \rightarrow |3d_{-\gamma}^1 4p^1 \underline{1s}\rangle \rightarrow |3d_{-\gamma}^1\rangle + \hbar\omega_f, \quad (67)$$

and schematically shown in Fig. 22(a). The one orbital excitation occurs at the site where the x ray is absorbed. (B) In the intermediate scattering state, one hole is created in the Mn $1s$ orbital. To screen the core hole potential, an electron comes from the NN O $2p$ orbital to the Mn site. Due to the hybridization between the O $2p$ and Mn $3d$ orbitals, this state strongly mixes with the state where the e_g orbitals in one of the NN Mn sites (j site) are empty. When the $4p$ electron fills the $1s$ orbital by emitting x ray, one of the $3d$ electrons in site i comes back to site j . This process is denoted by

$$|3d_{i\gamma_i}^1 3d_{j\gamma_j}^1\rangle + \hbar\omega_i \rightarrow |3d_{i\gamma_i}^1 3d_{i\gamma'_i}^1 \underline{1s}_i 4p_i^1\rangle \rightarrow |3d_{i\gamma'_i}^1 3d_{j\gamma'_j}^1\rangle + \hbar\omega_f, \quad (68)$$

and is shown in Fig. 22(b). Both one- and two-orbital excitations occur in i and j sites in this process. Since the process (B) arises from the higher order electronic processes of the electron hopping and Coulomb interaction, the process (A) is expected to be a dominant process of the orbital excitations in RIXS.

The scattering cross section of RIXS from the orbital excitations is obtained from Eq. (50) with Eq. (51) [211]. Here, the polarizability operator $\alpha_{l\alpha\beta}$ is expanded by operators for the electronic excitations in microscopic viewpoint. It is considered that the process (A) is dominant and the orbital excitations are caused by the off-diagonal Coulomb interaction $V_{\gamma-\gamma\alpha}$ given in Eq. (19). By using the Liouville operator method,

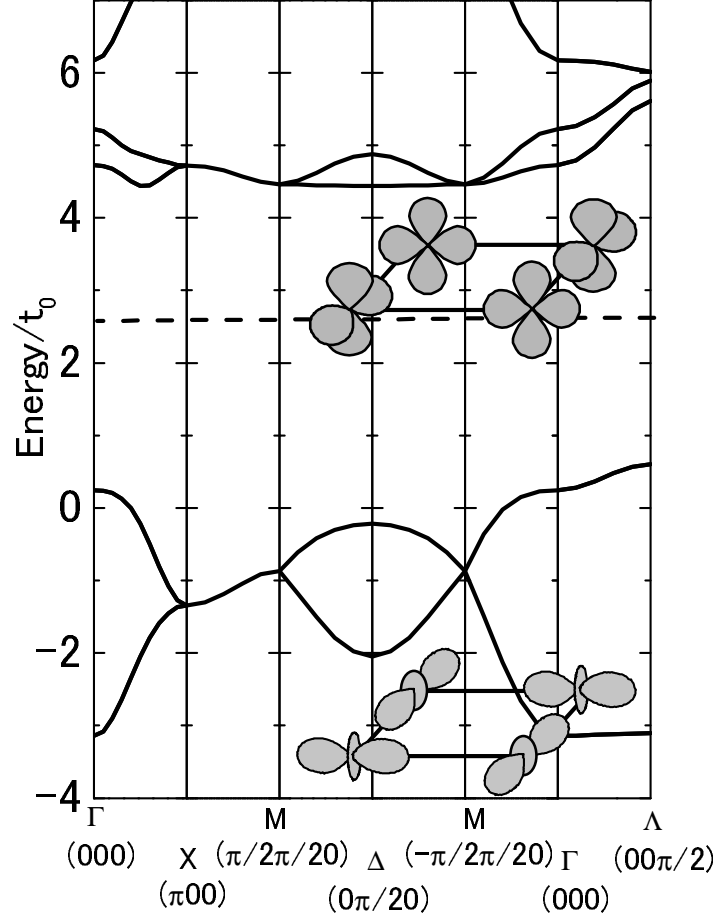


Figure 24. The electron energy bands for the $[d_{3x^2-r^2}/d_{3y^2-r^2}]$ -type orbital ordered state. The dotted line represents the chemical potential located at the center of the occupied and lowest unoccupied bands. The origin of the vertical axis is arbitrary. The inset shows schematic pictures of the orbital ordered states [211].

the explicit form of the polarizability is represented as

$$\alpha_{l\beta\alpha} = -\frac{|A_{1s4p}|^2}{m} \delta_{\alpha\beta} \sum_{\sigma_1\sigma_2} J_{l\alpha\sigma_2}^\dagger J_{l\alpha\sigma_1} \sum_{\sigma\gamma} T_{l\gamma\sigma} D_{\gamma\sigma\alpha}, \quad (69)$$

with $J_{l\alpha\sigma} = P_{l\alpha\sigma}^\dagger s_{l\sigma}$. $T_{l\gamma\sigma} (= T_{l+\sigma} + T_{l-\sigma})/2$ with $T_{l\mu\sigma} = \frac{1}{2} \sum_{\gamma\gamma'} d_{l\gamma\sigma}^\dagger(\sigma_\mu)_{\gamma\gamma'} d_{l\gamma'\sigma}$ represents a flipping of the pseudo-spin, and the factor $D_{\gamma\sigma\alpha}$ is an amplitude of the orbital excitations from the $3d_\gamma$ orbital to the $3d_{-\gamma}$ one by x ray with the polarization α . The final form of the scattering cross section is given by Eq. (50) with the Fourier transform of

$$\begin{aligned} \Pi_{\beta'\alpha'\beta\alpha}(t, \vec{r}_{l'} - \vec{r}_l) &= \frac{|A_{1s4p}|^4}{m^2} \delta_{\beta'\alpha'} \delta_{\beta\alpha} \sum_{\sigma\sigma'\gamma\gamma'} D_{\gamma'\sigma'\alpha'}^* D_{\gamma\sigma\alpha} \\ &\times \langle T_{l'x\sigma'}^\dagger(t) T_{lx\sigma}(0) \rangle. \end{aligned} \quad (70)$$

Consider RIXS in LaMnO_3 from the individual orbital excitations. The correlation function of $T_{lx\sigma}$ in Eq. (70) was calculated by applying the Hartree-Fock approximation to the generalized Hubbard model with orbital degeneracy.

The momentum dependence of the RIXS spectra is presented in Fig. 23 [211]. The energy parameters are the same with those in Fig. 15. The RIXS spectra do not have an intensity up to about $4t_0$ which corresponds to the Mott gap. A weak momentum dependence is seen in the RIXS spectra. The energy and momentum dependences of the RIXS spectra reflect the electronic band structure presented in Fig. 24. The occupied bands have the $d_{3x^2-r^2}$ and $d_{3y^2-r^2}$ orbital characters, the lowest unoccupied bands have the $d_{y^2-z^2}$ and $d_{z^2-x^2}$ orbital ones, and the Mott gap opens between these two. The main RIXS spectra in Fig. 23 are attributed to the transitions from the lower Hubbard band to the upper Hubbard band. Note that the lowest unoccupied bands show an almost flat dispersion, because electron hopping between the $d_{y^2-z^2}$ and $d_{z^2-x^2}$ orbitals is forbidden in the ab plane. This is the reason of the weak momentum dependence of RIXS spectra in comparison with that in cuprates [205]. The RIXS experiment was recently performed in LaMnO_3 in SPring-8 [209]. The mainly three peaks were observed around 2.5eV, 8eV and 11eV. The lowest peak around 2.5eV shows the momentum and azimuthal angle dependences and both are consistent with the theoretical calculations [212]. It was interpreted that this peak structure arises from the individual orbital excitations introduced above.

4. Summary

In this article, we review the recent theoretical and experimental studies of RXS in perovskite manganites and related compounds. The orbital degree of freedom in magnetic materials has been studied since more than 40 years ago. The recent discovery of CMR stimulates the intensive investigations based on the standpoint that orbital is the third degree of freedom of an electron in addition to spin and charge. However, the orbital degree of freedom and the orbital ordering remained hidden. The successful observations of the orbital ordering by RXS have uncovered this hidden degree of freedom and shown that this is not just theoretical hypotheses.

Through this review of the theoretical framework of RXS, we show that several characteristics of RXS are suitable to detect the orbital ordering. In particular, a tensor character of ASF is stressed. We introduce possible origins of the anisotropic ASF in orbital ordered state. The azimuthal angle dependence of the scattering intensity caused by this tensor character is crucial to identify the scattering from the orbital ordering. Beyond the microscopic description of ASF, it has been shown that the scattering cross section of RXS is represented by the correlation function of the pseudo-spin operators. This expression is applicable to study the orbital order-disorder phase transition. In addition to the RXS studies applied to the orbital ordering, we introduce the recent attempts to detect the dynamics of the orbital degree of freedom by RIXS. This method is not only the access to new kinds of excitations in solid but also provides a rich

information about origin of exotic electronic phenomena such as CMR. Through the recent rapid progresses of the synchrotron radiation source and related experimental technique, RXS may develop the orbital physics in correlated electron systems, as the neutron scattering has done in magnetic materials.

5. Acknowledgements

The authors would like to thank Y. Murakami, Y. Endoh, T. Arima, K. Hirota, D. Gibbs, J. P. Hill, M. Blume, J. Mizuki, T. Inami, S. Okamoto, H. Kondo and T. Hatakeyama. This work was supported by the Grant in Aid from Ministry of Education, Culture, Sports, Science and Technology of Japan, CREST, and Science and Technology Special Coordination Fund for Promoting Science and Technology. One of authors (S.M.) acknowledges support of the Humboldt Foundation.

References

- [1] Bednorz J G and Müller K A 1986 *Z. Phys.* **64** 189
- [2] Jonker G H and van Santen H 1950 *Physica* **16** 337
- [3] Jonker G H 1956 *Physica* **22** 707
- [4] Chahara K, Ohono T, Kasai M, Kanke Y and Kozono Y 1990 *Appl. Phys. Lett.* **62** 780
- [5] von Helmolt R, Wecker J, Holzapfel B, Schultz L and Samwer K 1993 *Phys. Rev. Lett.* **71** 2331
- [6] Tokura Y, Urushibara A, Moritomo Y, Arima T, Asamitsu A, Kido G and Furukawa N 1994 *J. Phys. Soc. Japan* **63** 3931
- [7] Jin S, Tiefel T H, McCormack M, Fastnacht R A, Ramesh R and Chen L H 1994 *Science* **264** 413
- [8] Millis A J, Littlewood P B and Shraiman B I 1995 *Phys. Rev. Lett.* **74** 5144
- [9] Millis A J, Shraiman B I and Mueller R 1996 *Phys. Rev. Lett.* **77** 175
- [10] Röder H, Zang J and Bishop A R 1996 *Phys. Rev. Lett.* **76** 1356 (1996)
- [11] Inoue J and Maekawa S 1995 *Phys. Rev. Lett.* **74** 3407
- [12] Tokura Y 2000 *Colossal Magnetoresistance Oxides* (Gordon and Breach, Amsterdam)
- [13] Kaplan T and Mahanti S D 1999 *Physics of Manganites* (Plenum Publishers)
- [14] Imada M, Fujimori A and Tokura Y 1998 *Rev. Mod. Phys.* **70** 1039
- [15] Moreo A, Yunoki S and Dagotto E 1999 *Science* **283** 2034
- [16] Tokura Y and Nagaosa N *Science* 2000 **288** 462
- [17] Zener C 1951 *Phys. Rev.* **82** 403
- [18] Anderson P W and Hasegawa H 1955 *Phys. Rev.* **100** 675
- [19] de Gennes P G 1960 *Phys. Rev.* **118** 141
- [20] Kubo K and Ohata N 1972 *J. Phys. Soc. Japan* **33** 21
- [21] Kubo K 1972 *J. Phys. Soc. Japan* **33** 929
- [22] Furukawa N 1996 *J. Phys. Soc. Japan* **64** 2734
- [23] Furukawa N 1996 *J. Phys. Soc. Japan* **64** 2754
- [24] Elemans J B A A, van Laar B, van der Veen K R and Loopstra B O 1971 *Jour. Soli. Stat. Chem.* **3** 238
- [25] Matsumoto G 1970 *J. Phys. Soc. Japan* **29** 606
- [26] Goodenough J B 1955 *Phys. Rev.* **100** 564
- [27] Mitchell J F, Argyriou D N, Potter C D, Hinks D G, Jorgensen J D and Bader S D 1996 *Phys. Rev. B* **54** 6172
- [28] Huang Q, Santoro A, Lynn J W, Erwin R W, Borchers J A, Peng J L and Greene R L 1997 *Phys. Rev. B* **55** 14987

- [29] Rodríguez-Carvajal J, Hennion M, Moussa F, Moudden A, Pinsard L and Revcolevschi A 1998 *Phys. Rev. B* **57** R3189
- [30] Wollan E O and Koehler W C 1955 *Phys. Rev.* **100** 545
- [31] Kugel K I and Khomskii D I 1973 *Sov. Phys. JETP* **37** 725
- [32] Hamada N, Sawada H and Terakura K 1995 *Spectroscopy of Mott insulators and correlated metals, Solid State Sciences 119*, (Springer-Verlag, Berlin)
- [33] Mizokawa T and Fujimori A 1995 *Phys. Rev. B* **51** 12880
- [34] Ishihara S, Inoue J and Maekawa S 1996 *Physica C* **263** 130
- [35] Ishihara S, Inoue J and Maekawa S 1997 *Phys. Rev. B* **55** 8280
- [36] Millis A J 1996 *Phys. Rev. B* **53** 8434
- [37] Solovyev I, Hamada N and Terakura K 1996 *Phys. Rev. Lett.* **76** 4825
- [38] Jiráček Z, Krupička S, Nekvasil V, Pollert E, Villeneuve G and Zounová F 1980 *J. Magn. Magn. Mater.* **15-18** 519
- [39] Tomioka Y, Asamitsu A, Moritomo Y, Kuwahara H and Tokura Y 1995 *Phys. Rev. Lett.* **74** 5108
- [40] Hwang H Y, Cheong S -W, Radaeli P G, Marezio M and Batlogg B 1995 *Phys. Rev. Lett.* **75** 914
- [41] Mori S, Chen C H, and Cheong S -W 1998 *Nature* **392** 473
- [42] Koshihara W, Kawamura Y, Ishihara S, Okamoto S, Inoue J and Maekawa S 1997 *J. Phys. Soc. Japan* **66** 957
- [43] Anisimov V I, Elfimov I S, Korotin M A and Terakura K 1997 *Phys. Rev. B* **55** 15 494
- [44] Solovyev I V and terakura K 1999 *Phys. Rev. Lett.* **83** 2825
- [45] Van Vleck J H 1953 *Rev. Mod. Phys.* **25** 220
- [46] Kanamori J 1959 *J. Phys. Chem. Solids* **10** 87
- [47] Roth L M 1966 *Phys. Rev.* **149** 306
- [48] Cyrot M and Lyon-Caen C 1975 *Jour. Physique* **36** 253.
- [49] Kugel K I and Khomskii D I 1972 *Sov. Phys.- JETP Letter* **15** 446
- [50] Kugel K I and Khomskii D I 1976 *Sov. Phys.- JETP Letter* **23** 237
- [51] Khomskii D I and Kugel K I 1973 *Solid State Commun.* **13** 763
- [52] Korovin L I and Kudinov E K 1975 *Sov. Phys. -Solid State* **16** 1666
- [53] Komarov A G, Korovin L I and Kudinov E K 1976 *Sov. Phys. -Solid State* **17** 1531
- [54] Inagaki S 1975 *J. Phys. Soc. Japan* **39** 596
- [55] Jahn H A and Teller E 1937 *Proc. Roy. Soc. A* **161** 220
- [56] Kanamori J 1960 *Jour. Appl. Phys. Suppl.* **31** 14S
- [57] Kataoka M and Kanamori J 1972 *J. Phys. Soc. Japan* **32** 113
- [58] Gehring G A and Gehring K A 1975 *Rep. Prog. Phys.* **38** 1
- [59] Kaplan M D and Vekhter B G 1995 *Cooperative Phenomena in Jahn-Teller Crystals* (Plenum Press, New York)
- [60] Feiner L F, Oleś A M and Zaanen J 1997 *Phys. Rev. Lett.* **78** 2799
- [61] Khaliullin G and Oudovenko V 1997 *Phys. Rev. B* **56** R14243
- [62] Feiner L F, Oleś A M and Zaanen J 1998 *J. Phys.: Condens. Matter* **10** L555
- [63] Khaliullin G and Kilian R 1999 *J. Phys.: Condens. Matter* **11** 9757
- [64] van den Brink J, Stekelenburg W, Khomskii D I, Sawatzky G A and Kugel K I 1998 *Phys. Rev. B* **58** 10276
- [65] Allen P B and Pereveinos V 1999 *Phys. Rev. Lett.* **83** 4828
- [66] Perebeinos V and Allen P B 1999 *Phys. Status Solidi (b)* **215** 607
- [67] Ishihara S, Yamanaka M and Nagaosa N 1997 *Phys. Rev. B* **56** 686
- [68] Shiba H, Shiina R and Takahashi A 1997 *J. Phys. Soc. Japan* **66** 941
- [69] Kilian R and Khaliullin G 1998 *Phys. Rev. B* **58** R11841
- [70] Mack F and Horsh P 1999 *Phys. Rev. Lett.* **82** 3160
- [71] Nakano H, Motome Y and Imada M 1999 *J. Phys. Soc. Japan* **68** 2178
- [72] Maezono R, Ishihara S and Nagaosa N 1998 *Phys. Rev. B* **57** R13993
- [73] Maezono R, Ishihara S and Nagaosa N 1998 *Phys. Rev. B* **58** 11583

- [74] van Veenendaal M and Fedro A J 1999 *Phys. Rev. B* **59** 1285
- [75] Sheng L and Ting C S 1999 *Phys. Rev. B* **60** 14 809
- [76] Okamoto S, Ishihara S and Maekawa S 2000 *Phys. Rev. B* **61** 14647
- [77] Koshibae W and Maekawa S 1999 *Physica C* **317-318** 205
- [78] Allen P B and Pereveinos V 1999 *Phys. Rev. B* **60** 10 747
- [79] van den Brink J, Horsh P and Oleś A M 2000 *Phys. Rev. Lett.* **85** 5174
- [80] Bala J, Sawatzky G A, Oleś A M, Macridin A 2001 *Phys. Rev. Lett.* **87** 067204
- [81] Yin W, Lin H and Gong C 2001 *Phys. Rev. Lett.* **87** 047204
- [82] Kilian R and Khaliullin G 1999 *Phys. Rev. B* **60** 13 458
- [83] Yunoki S, Moreo A and Dagotto E 1998 *Phys. Rev. Lett.* **81** 5612
- [84] Okamoto S, Ishihara S and Maekawa S 2000 *Phys. Rev. B* **61** 451
- [85] Hotta T, Takada Y, Koizumi H and Dagotto E 2000 *Phys. Rev. Lett.* **84** 2477
- [86] van den Brink J and Khomskii D I 2001 *Phys. Rev. B* **63** 140416
- [87] Takahashi A and Shiba H 2000 *J. Phys. Soc. Japan* **69** 3328
- [88] Maezono R and Nagaosa N 2000 *Phys. Rev. B* **62** 11576
- [89] Murakami Y, Kawada H, Kawata H, Tanaka M, Arima T, Moritomo H and Tokura Y 1998 *Phys. Rev. Lett.* **80** 1932
- [90] Ito Y and Akimitsu J 1976 *J. Phys. Soc. Japan* **40** 1333
- [91] Akimitsu J and Itoh Y 1976 *J. Phys. Soc. Japan* **40** 1642
- [92] Ichikawa H, Akimitsu J, Nishi M and Kakurai K 2000 *Physica B* **281&282** 482
- [93] Zuo J M, Kim M, O'Keefe M and Spence J C 1999 *Nature* **401** 49
- [94] Bricogne G 1988 *Acta Crystallogr. A* **44** 517
- [95] Takata M, Takeyama T, Sakata M, Sasaki S, Kodama K, Sato M, *Physics C* **263** 340
- [96] Takata M, Nishibori E, Kato K, Sakata M and Moritomo Y 1999 *J. Phys. Soc. Japan* **68** 2190
- [97] Templeton D H and Templeton L K 1980 *Acta Crystallogr. A* **36** 237
- [98] Templeton D H and Templeton L K 1982 *Acta Crystallogr. A* **38** 62
- [99] Templeton D H and Templeton L K 1985 *Acta Crystallogr. A* **41** 133
- [100] Templeton D H and Templeton L K 1985 *Acta Crystallogr. A* **41** 365
- [101] Kolpakov A V, Bushuev V A and Kuz'min R N 1978 *Sov. Phys. Usp.* **21** 959
- [102] Dmitrienko V E 1983 *Acta Crystallogr. A* **39** 29
- [103] Dmitrienko V E 1984 *Acta Crystallogr. A* **40** 89
- [104] Petcov A, Kirfel A and Eichhorn K 1990 *Acta Crystallogr. A* **46** 754
- [105] Kirfel A, Petcov A and Eichhorn K 1991 *Acta Crystallogr. A* **47** 180
- [106] Tsuji E, Kurasawa T, Yazawa I, Katoh H, Momozawa N, Ishida K and Kishimoto S 1996 *J. Phys. Soc. Japan* **65** 610
- [107] Nagano T, Kokubun J, Yazawa I, Kurasawa T, Kuribayashi M, Tsuji E, Ishida K, Sasaki S, Mori T, Kishimoto S and Murakami Y 1996 *J. Phys. Soc. Japan* **65** 3060
- [108] Materlik G, Sparks C J and Fischer K 1994 *Resonant Anomalous X-Ray Scattering* (Elsevier Science, Amsterdam)
- [109] Moritomo Y, Tomioka Y, Asamitsu A, Tokura Y and Matsui Y 1995 *Phys. Rev. B* **51** 3297
- [110] Bao W, Chen C H, Carter S A and Cheong S -W 1996 *Solid State Commun.* **98** 55
- [111] Sternlieb B J, Hill J P, Wildgruber U C, Luke G M, Nachumi B, Moritomo Y and Tokura Y 1996 *Phys. Rev. Lett.* **76** 2169
- [112] Murakami Y, Hill J P, Gibbs D, Blume M, Koyama I, Tanaka M, Kawata H, Arima T, Tokura Y, Hirota K and Endoh Y 1998 *Phys. Rev. Lett.* **81** 582
- [113] Fabrizio M, Altarelli M and Benfatto M 1998 *Phys. Rev. Lett.* **80** 3400: 1998 *Phys. Rev. Lett.* **81** E4030
- [114] Paolasini L, Vettier C, de Bergevin F, Yakhou F, Mannix D, Stunault A and Neubeck W 1999 *Phys. Rev. Lett.* **82** 4719
- [115] Nakamura K, Arima T, Nakazawa A, Wakabayashi Y and Murakami Y 1999 *Phys. Rev. B* **60** 2425

- [116] Endoh Y, Hirota K, Ishihara S, Okamoto S, Murakami Y, Nishizawa A, Fukuda T, Kimura H, Nojiri H, Kaneko K and Maekawa S 1999 *Phys. Rev. Lett.* **82** 4328
- [117] von Zimmermann M, Hill J P, Gibbs D, Blume M, Casa D, Keimer B, Murakami Y, Tomioka Y, and Tokura Y 1999 *Phys. Rev. Lett.* **83** 4872
- [118] Fukuda T, Hirota K, Kimura H, Murakami Y, Nishizawa A and Endoh Y 1999 *Japan. J. Appl. Phys. Suppl.* **38-1** 425.
- [119] Chatterji T, McIntyre G J, Caliebe W, Suryanarayanan R, Dhahlenne G and Revcolevschi A 2000 *Phys. Rev. B* **61** 570
- [120] Wakabayashi Y, Murakami Y, Koyama I, Kimura T, Tokura Y, Moritomo Y, Hirota K and Endoh Y 2000 *J. Phys. Soc. Japan* **69** 2731
- [121] von Zimmermann M, Nelson C S, Hill J P, Gibbs D, Blume M, Casa D, Keimer B, Murakami Y, Kao C -C, Venkataraman C, Gog T, Tomioka Y and Tokura Y 2001 *Phys. Rev. B* **64** 195133
- [122] von Zimmermann M, Nelson C S, Kim Y -J, Hill J P, Gibbs D, Nakao H, Wakabayashi Y, Murakami Y, Tomioka Y, Tokura Y, Arima T, Kao C -C, Casa D, Venkataraman C and Gog T 2001 *Phys. Rev. B* **64** 064411
- [123] Wakabayashi Y, Murakami Y, Moritomo Y, Koyama I, Nakao H, Kiyama T, Kimura T, Tokura Y and Wakabayashi N 2001 *J. Phys. Soc. Japan* **70** 1194
- [124] Kiyama T, Murakami Y, Nakao H, Wakabayashi Y, Izumi M, Kawasaki M and Tokura Y (unpublished).
- [125] Hirota K, Cox DE, Fukuda T, Murakami Y and Endoh Y 2001 *Bulletin of the American Physical Society* **46** 265
- [126] Keimer B, Casa D, Ivanov A, Lynn J W, von Zimmermann M, Hill J P, Gibbs D, Taguchi K and Tokura Y 2000 *Phys. Rev. Lett.* **85** 3946
- [127] Noguchi M, Nakazawa A, Oka S, Arima T, Wakabayashi Y and Murakami Y 2000 *Phys. Rev. B* **62** R9271
- [128] Nakao H, Wakabayashi Y, Kiyama T, Murakami Y, von Zimmermann M, Hill J P, Gibbs D, Ishihara S, Taguchi K and Tokura Y (unpublished).
- [129] Tanaka Y, Inami T, Nakamura T, Yamauchi H, Onodera H, Ohoyama K and Yamaguchi Y 1999 *J. Phys.: Condens. Matter* **11** L505
- [130] Hirota K, Oumi N, Matsumura T, Nakao H, Wakabayashi Y, Murakami Y and Endoh Y 2000 *Phys. Rev. Lett.* **84** 2706
- [131] McMorrow D F, McEwen K A, Steigenberger U, Rønnow H M and Yakhou F 2001 *Phys. Rev. Lett.* **87** 057201
- [132] Nakao H, Magishi K, Murakami Y, Koyama K, Hirota K, Endoh Y and Kunii S 2001 *J. Phys. Soc. Japan* **70** 1857
- [133] Matsumura T, Oumi N, Hirota K, Nakao H, Murakami Y, Wakabayashi Y, Arima T, Ishihara S and Endoh Y (unpublished) cond-mat/0011033
- [134] Ishihara S and Maekawa S 1998 *Phys. Rev. Lett.* **80** 3799
- [135] Ishihara S and Maekawa S 1998 *Phys. Rev. B* **58** 13442
- [136] Ishihara S and Maekawa S 2000 *Phys. Rev. B* **62** 5690
- [137] Ishihara S and Maekawa S 2000 *Phys. Rev. B* **62** R9252
- [138] Ishihara S and Maekawa S 2001 *J. Magn. Magn. Mater.* **233** 21
- [139] Ishihara S, Hatakeyama T and Maekawa S 2001 (unpublished)
- [140] Elfimov I S, Anisimov V I and Sawatzky G A 1999 *Phys. Rev. Lett.* **82** 4264
- [141] Benfatto M, Joly Y and Natoli C R 1999 *Phys. Rev. Lett.* **83** 636
- [142] Takahashi M, Igarashi J and Fulde P 1999 *J. Phys. Soc. Japan* **68** 2530
- [143] Takahashi M, Igarashi J and Fulde P 2000 *J. Phys. Soc. Japan* **69** 1614
- [144] Takahashi M and Igarashi J 2001 *Phys. Rev. B* **64** 075110
- [145] Nagao T and Igarashi J (unpublished) cond-mat/0107377
- [146] Ovchinnikova E N and Dmitrienko V E 2000 *Acta Crystallogr. A* **56** 2
- [147] Castleton C W M and Altarelli M 2000 *Phys. Rev. B* **62** 1033

- [148] Shishidou T, Jo T and Oguchi T (preprint)
- [149] Benedetti P, van den Brink J, Pavarini E, Vigliante A and Wochner P 2001 *Phys. Rev. B* **63**, 060408(R)
- [150] Mahadevan P, Terakura K and Sarma D D 2001 *Phys. Rev. Lett.* **87** 066404
- [151] Inami T, Ikeda N, Murakami Y, Koyama I, Wakabayashi Y and Yamada Y 1999 *Japan. J. Appl. Phys. Suppl.* **38-1** 212
- [152] Garcia J, Subias G, Proietti M G, Renevier H, Joly Y, Hodeau J L, Blaso J, Sanchez M C and Bèrar J F *Phys. Rev. Lett.* **85** 578
- [153] Nakao H, Ohwada K, Takesue N, Fujii Y, Isobe M, Ueda Y, von Zimmermann M, Hill J P, Gibbs D, Woicik J C, Koyama I and Murakami Y 2000 *Phys. Rev. Lett.* **85** 4349
- [154] Yamada Y, Hino O, Nohdo S, Kanao R, Inami T and Katano S 1996 *Phys. Rev. Lett.* **77** 904
- [155] Kawano H, Kajimoto R and Yoshizawa H 1996 *Phys. Rev. B* **53** R14 709
- [156] Argyriou D N, Mitchell J F, Potter C D, Hinks D G, Jorgensen J D and Bader S D 1996 *Phys. Rev. Lett.* **76** 3826
- [157] Dabrowski B, Xiong X, Bukowski Z, Dybzinski R, Klamut P W, Siewenie J E, Chmaissem O, Shaffer J, Kimball C W, Jorgensen J D and Short S 1999 *Phys. Rev. B* **60** 7006
- [158] Nojiri H, Kaneko K, Motokawa M, Hirota K, Endoh Y and Takahashi K 1999 *Phys. Rev. B* **60** 4142
- [159] Cox D E, Iglesias T, Moshopoulou E, Hirota K, Takahashi K and Endoh Y 2001 *Phys. Rev. B* **64** 024431
- [160] Tokura Y, Tomioka Y, Kuwahara H, Asamitsu A, Moritomo Y and Kasai M 1996 *J. Appl. Phys.* **79** 5288
- [161] Sakurai J J 1987 *Advanced Quantum Mechanics* (Addison-Wesley, Massachusetts)
- [162] Blume M 1985 *J. Appl. Phys.* **57** 3615
- [163] Lovesey S W 1993 *Rep. Prog. Phys.* **56** 257
- [164] Forster D 1990 *Hydrodynamic Fluctuations, Broken Symmetry and Correlation Functions* (Addison-Wesley, Massachusetts)
- [165] Fulde P 1993 *Electron Correlations in Molecules and Solids* (Springer-Verlag, Berlin)
- [166] Matsumoto H, Sasaki M, Ishihara S and Tachiki M 1992 *Phys. Rev. B* **46** 3009
- [167] Kosugi N, Kondoh H, Tajima H and Kuroda H 1989 *Chemical Physics* **135** 149
- [168] Tranquada J M, Heald S M, Kunnmann W, Moodenbaugh A R, Qiu S L and Xu Y 1991 *Phys. Rev. B* **44** 5176
- [169] Tolentino H, Medarde M, Fontaine A, Baudelet F, Dartyge E, Guay D and Tourillon G 1992 *Phys. Rev. B* **45** 8091
- [170] Sahiner A, Croft M, Guha S, Perez I, Zhang Z, Greenblatt M, Metcalf P A, Jahns H and Liang G 1995 *Phys. Rev. B* **51** 5879
- [171] Sahiner A, Croft M, Zhang Z, Greenblatt M, Perez I, Metcalf P, Jhans H, Liang G and Jeon Y 1996 *Phys. Rev. B* **53** 9745
- [172] Croft M, Sills D, Greenblatt M, Lee C, Cheong S -W, Ramanujachary K V and Tran D 1997 *Phys. Rev. B* **55** 8726
- [173] Wu Z, Benfatto M and Natoli C R 1996 *Phys. Rev. B* **54** 13409
- [174] Hill J P, Kao C -C, Caliebe W A L, Matsubara M, Kotani A, Peng J L and Greene R L 1998 *Phys. Rev. Lett.* **80** 4976
- [175] Saitoh T, Bocquet A E, Mizokawa T, Namatame H, Fujimori A, Abbate M, Takeda Y and Takano Y 1995 *Phys. Rev. B* **51** 13942
- [176] Park J -H, Chen C T, Cheong S -W, Bao W, Meigs G, Chakarian V and Idzerda Y U 1996 *Phys. Rev. Lett.* **76** 4215
- [177] Chainani A, Mathew M and Sarma D D 1993 *Phys. Rev. B* **47** 15397
- [178] Ezhov S Y, Anisimov V I, Khomskii D I and Sawatzky G A 1999 *Phys. Rev. Lett.* **83** 4136
- [179] Mila F, Shiina R, Zhang F -C, Joshi A, Ma M, Anisimov V and Rice T M 2000 *Phys. Rev. Lett.* **85** 1714

- [180] Di Matteo S, Perkins M B and Natoli C R (unpublished) cond-mat/0107026
- [181] Moritomo Y, Asamitsu A, Kuwahara H and Tokura Y 1996 *Nature (London)* **380** 141
- [182] Kimura T, Tomioka Y, Asamitsu A and Tokura Y 1998 *Phys. Rev. Lett.* **81**, 5920
- [183] Kubota M, Fujioka H, Hirota K, Ohoyama K, Moritomo Y, Yoshizawa H and Endoh Y 2000 *J. Phys. Soc. Japan* **69** 1606
- [184] Medarde M, Mitchell J F, Millburn J E, Short S and Jorgensen J D 1999 *Phys. Rev. Lett.* **83** 1223
- [185] Ling C D, Millburn J E, Mitchell J F, Argyriou D N, Linton J and Bordallo H N 2000 *Phys. Rev. B* **62** 15096
- [186] Ishihara S, Okamoto S and Maekawa S 1997 *J. Phys. Soc. Japan* **66** 2965
- [187] Okamoto S, Ishihara S and Maekawa S 2001 *Phys. Rev. B* **63** 104401
- [188] Hirota K, Ishihara S, Fujioka H, Kubota M, Yoshizawa Y, Moritomo Y, Endoh Y and Maekawa S *Phys. Rev. B* (to appear) cond-mat/0104535
- [189] Chuang Y -D, Gromko A D, Dessau D S, Kimura T and Tokura Y 2001 *Science* **292** 1509
- [190] Moriya T 1967 *J. Phys. Soc. Japan* **23** 28
- [191] Sakai O and Tachiki M 1978 *J. Phys. Chem. Solids* **39** 269
- [192] Shastry B S and Shraiman B I 1990 *Phys. Rev. Lett.* **65** 1068
- [193] Kataoka M and Endoh Y 1980 *J. Phys. Soc. Japan* **48** 912
- [194] Terauchi H, Mori M and Yamada Y 1972 *J. Phys. Soc. Japan* **32** 1049
- [195] Kirvoglaz M A 1996 *Diffuse Scattering of X-Rays and Neutrons by Fluctuations* (Springer-Verlag, Berlin Heidelberg)
- [196] Inoue J, Okamoto S, Ishihara S, Koshibae W, Kawamura Y and Maekawa S 1997 *Physica B* **237-238** 51
- [197] Saitoh E, Okamoto S, Takahashi K T, Tobe K, Yamamoto K, Kimura T, Ishihara S, Maekawa S and Tokura Y 2001 *Nature* **410** 180
- [198] Okamoto S, Ishihara S and Maekawa S (unpublished) cond-mat/0108032
- [199] Ederer D L and McGuire J H 1996 *Raman emission by x-ray scattering* (World Scientific, Singapore)
- [200] Gel'mukhanov F and Ågren H 1999 *Physics Report* **312** 87
- [201] Kotani A and Shin S 2001 *Rev. Mod. Phys.* **73** 203
- [202] Isaacs E D, Platzman P M, Metcalf P and Honig J M 1996 *Phys. Rev. Lett.* **76** 4211
- [203] Platzman P M and Isaacs E D 1998 *Phys. Rev. B* **57** 11107
- [204] Abbamonte P, Burns C A, Isaacs E D, Platzman P M, Miler L L, Cheong S -W and Klein M V 1999 *Phys. Rev. Lett.* **83** 860
- [205] Hasan M Z, Isaacs E D, Shen Z -X, Miller L L, Tsutsui K, Tohyama T and Maekawa S 1999 *Science* **288** 1811
- [206] Ma Y J and Blume M 1995 *Rev. Sci. Instrum.* **66** 1543
- [207] Tsutsui K, Tohyama T and Maekawa S 2000 *Phys. Rev. Lett.* **83** 3705
- [208] Tsutsui K, Tohyama T and Maekawa S 2000 *Phys. Rev. B* **61** 7180
- [209] Inami T, Fukuda T, Mizuki J, Nakao H, Matsumura T, Murakami Y, Hirota K and Endoh Y 2001 *Nucl. Inst. and Meth. Phys. Res. A* **467-468** 1081
- [210] Ishihara S and Maekawa S 2000 *Phys. Rev. B* **62** 2338
- [211] Kondo H, Ishihara S and Maekawa S 2001 *Phys. Rev. B* **64** 014414
- [212] Inami T, Ishihara S, Kondo H, Mizuki J, Fukuda T, Maekawa S, Nakao H, Matsumura T, Hirota K, Murakami Y and Endoh Y (unpublished) cond-mat/0109509